Research Square

Preprints are preliminary reports that have not undergone peer review.
They should not be considered conclusive, used to inform clinical practice,
or referenced by the media as validated information.

Nanoscale Defect Modulation in Zn 1-x Ni x Fe 2 O 4 Spinel Nanoparticles: Hydrodynamic Agglomeration, Mesoporosity, and Coupled Magnetic and Electrochemical Responses

I. Dominic Xavier
St. Joseph's College of Arts and Science
R. Sagayaraj
sagayarajnancy@gmail.com

St. Joseph's College of Arts and Science
A. Maria Bernadette Leena
Holy Cross College (Autonomous)
N. Lavanya
A.D.M.College for Women
C. Yogambal
IFET College of engineering
A. Amalorpavadoss
St. Joseph's College of Arts and Science
S. Sebastian
St. Joseph's College of Arts and Science
S. Aravazhi
Arignar Anna Government Arts College

Research Article

Keywords: Spinel nanoparticles, Spinel ferrites, Mesoporous, Grain-boundary pinning, Cation distribution, Soft ferrimagnetic, Hydrodynamic agglomeration, Faradaic charge storage

Posted Date: August 31st, 2026

DOI: https://doi.org/10.21203/rs.3.rs-10216821/v1

License: This work is licensed under a Creative Commons Attribution 4.0 International License.
Read Full License

Additional Declarations:
No competing interests reported.

Table 1 to 7 are available in the Supplementary Files section.

Nanoscale Defect Modulation in $Zn_{1-x}Ni_xFe_2O_4$ Spinel Nanoparticles: Hydrodynamic Agglomeration, Mesoporosity, and Coupled Magnetic and Electrochemical Responses

I. Dominic Xavier [a], R. Sagayaraj [a*], A. Maria Bernadette Leena [b], N. Lavanya [c], C. Yogambal [d], A. Amalorpavadoss [e], S. Sebastian [a], S. Aravazhi [f]

[a] PG & Research Department of Physics, St. Joseph's College of Arts and Science (Autonomous), Cuddalore-607001, Affiliated to Annamalai university, Tamil Nadu, India

[b] PG & Research Department of Physics, Holy Cross College (Autonomous), Tiruchirappalli 2, Affiliated to Bharathidasan University, Tiruchirappalli, Tamil Nadu, India

[c] Department of Physics, A.D.M.College for Women, (Autonomous and Affiliated to Bharathidasan University, Tiruchirappalli), Nagapattinam- 611001, Tamil Nadu, India

[d] PG & Research Department of Chemistry, St. Joseph's College of Arts and Science (Autonomous), Cuddalore-607001, Affiliated to Annamalai university, Tamil Nadu, India

[e] Department of Physics, IFET College of engineering, Gangarampalayam, Villupuram-605108, Tamil Nadu, India

[f] PG & Research Department of Physics, Arignar Anna Government Arts College, Affiliated to Annamalai university, Villupuram, Tamilnadu, 605602, India

Abstract

Spinel ferrites ($Zn_{1-x}Ni_xFe_2O_4$) exhibit adjustable magnetic and electrical properties, which are influenced by the distribution of cations between the tetrahedral and octahedral sites. XRD confirmed cubic spinel structure formation with systematic lattice contraction from 8.485 Å (x=0.00) to 8.451 Å (x=0.02), followed by a pronounced anomaly at x=0.03 (a=8.522 Å) and relaxation at x=0.04 (8.462 Å). The x=0.03 composition exhibited the minimum crystallite size (19.7 nm) and maximum microstrain (0.0058), consistent with the heightened defect density and cation redistribution. FTIR showed characteristic spinel bands (ν_1= 547–550 cm^{-1}, ν_2= 451–460 cm^{-1}) and Kt>Ko (2.19–2.22×10^5 vs. 1.49–1.55×10^5 dyne/cm), alongside minor signatures of adsorbed water/CO_2 and trace amounts of PVA residues. The EIS Nyquist spectra displayed a single depressed semicircle dominated by grain boundaries; the fitted R_{gb} peaked

at 11119.0 Ω at x=0.03 with non-Debye behavior (θ=36.75°–44.73°, n up to 0.592), indicating maximal boundary scattering and suppressed Fe^{2+}/Fe^{3+} hopping. Despite nanoscale primary sizes, DLS revealed severe aqueous agglomeration (Z-average 3006–4539.9 nm; PDI 0.907–1.270), maximized at x=0.03 (4539.9 nm; diffusion minimum 1.084×10^{-9} cm^2/s), consistent with FE-SEM observations of porous spherical agglomerates formed via PVA combustion and gas evolution. Electrochemically, CV at 10 mV s^{-1} showed a shift from an anodic peak (123.3 mV, 1.548 μA for x=0.00) to cathodic-dominated redox (−146.9 to −338.6 mV) upon Ni substitution; specific capacitance dropped at x=0.01, then increased to 6.47 and 6.24 mF g^{-1} at x=0.02 and 0.03 before declining to 3.14 mFg^{-1} at x=0.04, attributed to defect-rich mesoporosity and enlarged electroactive interface. VSM indicated soft ferrimagnetic/near-superparamagnetic behavior (Mr/Ms=0.0033–0.0529) with a critical x=0.03 hardening: Ms sharply decreased to 23.087×10^{-3} emu g^{-1}, while Hc rose to 150.0 Oe and K to 1.732 erg g^{-1}, implicating dead-layer spin canting and defect/grain-boundary pinning. Overall, a narrow compositional threshold near x=0.03 maximizes the defect density and grain-boundary networks, simultaneously enhancing the coercivity and optimizing faradaic charge storage, establishing low-concentration Ni doping as an effective strategy to co-tune the magnetic functionality and electrochemical energy-storage performance in Zn-ferrite nanomaterials.

Keywords

Spinel nanoparticles; Spinel ferrites; Mesoporous; Grain-boundary pinning; Cation distribution; Soft ferrimagnetic; Hydrodynamic agglomeration; Faradaic charge storage

*Corresponding Author:

E-Mail: sagayarajnancy@gmail.com (R. SAGAYARAJ)

1 Introduction

Ferrites are an important class of magnetic materials with the general formula MFe_2O_4, where M represents a divalent metal ion such as Zn^{2+}, Ni^{2+}, or Co^{2+} [1]. These materials exhibit ferrimagnetic behavior, high electrical resistivity, and low eddy current losses, making them suitable for high-frequency applications [2]. Spinel ferrites have a cubic structure with tetrahedral (A) and octahedral (B) sites, and their properties depend strongly on the distribution of cations among these sites [3]. Ferrite materials have three types of spinel structures: normal

spinel, inverse spinel, and mixed spinel [4]. Among spinel ferrites, zinc ferrite ($ZnFe_2O_4$) and nickel ferrite ($NiFe_2O_4$) have gained significant attention owing to their unique structural, magnetic, and electrical properties [5, 6]. $ZnFe_2O_4$ is a normal spinel ferrite in which Zn^{2+} ions occupy tetrahedral (A) and Fe^{3+} ions occupy octahedral (B) sites. It crystallizes in a cubic structure with the space group Fd-3m [7]. In bulk form, $ZnFe_2O_4$ exhibits antiferromagnetic behavior at low Néel temperatures. However, when synthesized in the nanoparticle form, it exhibits superparamagnetic or weak ferromagnetic behavior owing to cation redistribution and surface effects. This is mainly caused by the partial migration of Fe^{3+} ions into the A-sites, resulting in strong A–B exchange interactions [8–10]. $ZnFe_2O_4$ possesses high chemical stability, high electrical resistivity, and low magnetic loss, making it suitable for high-frequency and electronic applications [11–13]. $ZnFe_2O_4$ is widely used in chemical reactions because of its large surface area and catalytic activity [14]. $NiFe_2O_4$ is an inverse spinel ferrite, where Fe^{3+} ions are distributed equally between the A and B sites, and Ni^{2+} ions occupy the octahedral (B) sites [6]. The structure is represented as, $NiFe_2O_4$ exhibits ferrimagnetic behavior with a high Curie temperature (850 K), making it suitable for magnetic and electronic applications. It has a high saturation magnetization, moderate coercivity, and high resistivity, which reduce eddy current losses [15]. At the nanoscale, $NiFe_2O_4$ exhibits enhanced magnetic properties owing to quantum size effects and surface spin disorder, improving its performance in advanced applications [16]. Normal and inverse spinel materials have various compositions, resulting in distinct modifications to their structural and magnetic parameters [17, 18]. $Zn_{1-x}Ni_xFe_2O_4$ belongs to the Ni–Zn ferrite family, which is a class of spinel ferrites that combines good chemical stability with useful magnetic behavior at the nanoscale [19, 20]. The reported synthesis routes for these nanoparticles include co-precipitation, hydrothermal/solvothermal processing, sol-gel methods, citrate-gel processes, reverse micelle or micro-emulsion methods, microwave combustion, citrate precursor routes, sonochemical synthesis, thermal plasma synthesis, solid-state methods, and soft-chemistry methods [19, 21–30].These methods are used because they can control the particle size, morphology, and crystallinity, which shape the final magnetic response of the material. Among these routes, the hydrothermal and solvothermal methods are commonly used for Ni–Zn ferrites because they avoid expensive starting materials, harsh solvents, and very high temperatures or pressures, while still allowing control over the nanosphere size and crystal features. Simple thermal treatment approaches are also attractive because they only require metal nitrates, water, and a capping agent, such as PVP, which makes the process low-cost, fairly low-temperature, and environmentally friendly [12, 25]. Structurally, Zn-Ni ferrites are based on a cubic spinel

framework. In bulk form, zinc ferrite is a normal spinel with Zn^{2+} mainly on tetrahedral A sites and Fe^{3+} on octahedral B sites, whereas nickel ferrite is an inverse spinel with Ni^{2+} preferentially occupying the B sites [5]. In Ni–Zn ferrite nanoparticles, Zn generally prefers the A sites, and Ni prefers the B sites, with Fe^{3+} being shared between both [25]. This mixed-site occupancy is central to the ability to tune the properties of Zn-Ni ferrite nanoparticles by changing their composition and synthesis conditions [25, 31]. A broad trend from ferrite nanoparticle studies is that synthesis and post-treatment strongly affect the crystal quality, and higher annealing or calcination temperatures usually increase the particle size, reduce defects, and improve crystallinity, whereas cation substitution can shift the lattice parameters and slightly distort the structure. For $ZnFe_2O_4$ -based nanoparticles, the addition of magnetic cations such as Ni^{2+} in place of nonmagnetic Zn^{2+} is known to tune both the structure and magnetism, which is the main reason $Zn_{1-x}Ni_xFe_2O_4$ has been widely explored [12, 31]. This is one of the most common routes for synthesizing Ni–Zn ferrite nanoparticles because it is simple, low-cost, can be performed at near-ambient or mild temperatures, and usually yields narrow particle size distributions. It is widely used to prepare Ni–Zn ferrites and Zn-ferrite nanoparticles [25, 32, 33]. Direct examples include Zn–Ni ferrite nanoparticles made by coprecipitation followed by annealing at 200–1000 °C, where annealing increased the crystallite size and improved the dispersion [34]. Related work on Zn ferrite shows that surfactants such as PVP can be added during co-precipitation to help control morphology, and microwave assistance can speed up the precipitation process while keeping it low-cost and greener [35, 36]. Hydrothermal/solvothermal processing is widely used for Ni–Zn ferrites because it does not require very high temperatures or pressures and avoids expensive starting materials and harsh solvents [22, 25]. A clear example is the monodisperse $Ni_{0.5}Zn_{0.5}Fe_2O_4$ nanospheres synthesized by a simple solvothermal route, where the reactant concentration was used to tune the nanosphere size from 238 to 35 nm [25]. Hydrothermal preparation has also been used for Ni-doped zinc ferrite nanopowders, producing cubic-structured samples that were later studied for their magnetic properties and antimicrobial activities [37]. Solvothermal methods can also be combined with microwave heating to shorten long reflux-based syntheses from hours to minutes while still producing phase-pure Zn ferrite nanoparticles [38]. Sol-gel is a standard wet-chemical route used across Ni–Zn ferrites because it gives good chemical mixing and often good control of crystallization after calcination. It has been repeatedly listed as one of the main synthesis methods for Ni–Zn and Zn ferrite nanoparticles [25, 39–41]. The sol-gel method can also be combined with microwave heating. For example, microwave-assisted sol-gel synthesis has been used to produce size-monodispersed spherical Zn-ferrite

nanoparticles [42]. Comparative studies on related Ni-containing ferrites show that co-precipitation and sol-gel can lead to different crystallite size trends with composition; therefore, the route itself matters, not just the target composition [43]. These routes are used when tighter control over the nanoscale reaction space is required. These methods are listed among the established methods for Ni–Zn ferrite nanoparticle synthesis [25, 31, 41]. For $Zn_{1-x}Ni_xFe_2O_4$, synthesis in microemulsions yielded smaller particles and allowed single-phase product formation at a lower treatment temperature of 400 °C compared to stepwise precipitation at 600 °C [26]. Thermal decomposition is another practical route for synthesizing Ni–Zn ferrites, and it is often chosen when uniform, fine, and highly crystalline nanoparticles are required. $Zn_{1-x}Ni_xFe_2O_4$ nanoparticles (x = 0.5) to 0.7 were successfully synthesized as pure spinel ferrites with sizes of approximately 46–51 nm [44]. More broadly, thermal decomposition is a conventional synthesis method that has been mentioned repeatedly in the literature on ferrites [41]. A low-complexity variant of Ni–Zn ferrites uses only metal nitrates in water, along with PVP as a capping agent, followed by drying and calcination. This route is noted for its simplicity, low cost, moderate calcination temperature, and low waste generation rate [31]. Using this method, $Ni_{0.25}Zn_{0.75}Fe_2O_4$ nanoparticles were produced with an average size increasing from 7 to 25 nm as the calcination temperature increased from 723 to 873 K [31]. $Zn_{1-x}Ni_xFe_2O_4$ nanoparticles below 10 nm were prepared by combining chemical precipitation with high-energy ball milling and compared with thermally synthesized analogs [44, 45]. In that study, ferrites containing zinc were formed after 3 h of mechanical treatment, whereas pure $NiFe_2O_4$ required 6 h, showing that milling time can affect phase formation [45]. Although wet-chemical routes dominate nanoscale work, solid-state or solid-reaction methods have also been used. These include conventional solid-state reactions and milling-assisted solid-state reactions, followed by high-temperature sintering [12, 41, 46]. A $NiFe_2O_4$ example used oxide powders, 5 h milling, and sintering at 1200 °C for 3 h to obtain a single-phase material at the $NiFe_2O_4$ composition [46]. Structurally, Zn–Ni ferrite nanoparticles are built on a spinel lattice, which is often described as a face-centered cubic oxygen framework with cations distributed over tetrahedral A and octahedral B sites in the lattice. For the Ni–Zn ferrite system, Zn^{2+} generally prefers A sites, Ni^{2+} prefers B sites, and Fe^{3+} occupies both; therefore, the nanoparticles are best viewed as mixed spinels rather than a simple end-member [25, 31]. In practice, XRD is the main tool used to confirm phase formation, and most reported $Zn_{1-x}Ni_xFe_2O_4$ nanopowders show a single-phase cubic spinel structure after suitable heat treatment or optimized wet-chemical synthesis. This has been reported for solvothermal $Ni_{0.5}Zn_{0.5}Fe_2O_4$, thermally decomposed $Zn_{1-x}Ni_xFe_2O_4$, sol-gel auto-combustion $Zn_{1-x}Ni_xFe_2O_4$, co-precipitated

and annealed Zn–Ni ferrites, hydrothermal Ni-doped zinc ferrite, and microemulsion-made $Zn_{1-x}Ni_xFe_2O_4$[25, 26, 34, 44, 47]. However, nanoscale zinc ferrite does not always maintain an ideal bulk cation order at room temperature. Several $ZnFe_2O_4$ studies have found mixed or partially inverted spinel characteristics, with Fe^{3+} present on both the A- and B-sites [42]. Random or redistributed Zn/Fe occupation has also been used to explain the room-temperature ferromagnetic behavior of nanosized $ZnFe_2O_4$ [36, 42, 48]. The synthesis conditions strongly affect the lattice size. A common trend is that increasing the Zn content expands the unit cell, which fits the larger ionic size of Zn^{2+} compared with Ni^{2+}. This increase in the lattice parameter was also observed in thermally decomposed $Zn_{1-x}Ni_xFe_2O_4$, microemulsion/precipitation-made $Ni_{1-x}Zn_xFe_2O_4$, and earlier Ni–Zn ferrite nanoparticle studies [26, 31, 44, 49, 50]. The XRD peak shifts with composition also supported this trend. In sol-gel auto-combustion $Zn_{1-x}Ni_xFe_2O_4$, increasing Zn from 0.25 to 0.75 shifted the peaks to shorter angles and gave lattice constants of 8.351–8.434 Å [47]. The crystallite size is also highly dependent on the synthesis method. In Zn–Ni ferrites prepared by coprecipitation and annealing, the crystallite size increased from 15.1 to 25.1 nm as the annealing temperature reached 1000 °C. In the simple nitrate/PVP thermal-treatment route for $Ni_{0.25}Zn_{0.75}Fe_2O_4$, the average particle size increased from 7 to 25 nm when the calcination temperature was increased from 723 to 873 K. The sol-gel auto-combustion samples covered an even wider crystallite size range of approximately 17.55–66.98 nm, depending on the composition and annealing [31, 34, 47]. This broader pattern, in which higher annealing temperatures yielded larger particles and better crystallinity with fewer defects, is consistent with the zinc ferrite literature [12, 51]. Microemulsion-made $Ni_{1-x}Zn_xFe_2O_4$formed a single phase at a lower temperature and produced smaller particles with a higher lattice strain than that of the stepwise precipitation method, even though their unit cell parameters were similar. In a separate hybrid route, ferrites containing Zn were formed after 3 h of high-energy milling, whereas pure $NiFe_2O_4$ required 6 h, indicating that the composition changes the kinetics of spinel formation [26, 45]. The morphology is usually nanospherical to near-spherical; however, aggregation is prevalent. Transmission electron microscopy (TEM) and scanning electron microscopy (SEM) revealed spherical $ZnFe_2O_4$ nanoparticles, nearly spherical $Ni_{1-x}Zn_xFe_2O_4$ particles, and $Ni_{0.5}Zn_{0.5}Fe_2O_4$ nanospheres with diameters that could be tuned from 238 to 35 nm by changing the reactant concentration. Other syntheses yielded self-assembled sub-microspheres built from (approximately)11 nm $ZnFe_2O_4$ grains or showed noticeable agglomeration in hydrothermal Ni-doped zinc ferrite powders [25, 35, 40, 47]. The FTIR data supported the spinel assignment by showing typical metal–oxygen bands from the tetrahedral and octahedral sites. The reported

bands include features near 540–550 and 455–470 cm^{-1} for $ZnFe_2O_4$, and near 555 and 378 cm^{-1} for Zn–Ni ferrite, both of which are consistent with spinel-site vibrations [34, 35, 52]. Overall, the key structural message is that $Zn_{1-x}Ni_xFe_2O_4$ nanoparticles usually form a cubic spinel phase, but their real nanoscale structure depends on the synthesis: the composition shifts the lattice parameter, heat treatment grows crystals and improves ordering, and the route choice changes the strain, agglomeration, and degree of inversion or cation redistribution. These structural details are important because they directly determine the magnetic response, as discussed in the next section [25, 26, 34, 47]. The magnetic behavior of Zn–Ni ferrite nanoparticles is strongly tied to the fact that they are nanoscale mixed spinels, in which Zn^{2+}, Ni^{2+}, and Fe^{3+} do not contribute equally to the A and B sites. Several studies have explicitly linked the measured saturation magnetization to the cation distribution, and in the $Zn_{1-x}Ni_xFe_2O_4$ system, the Fe^{3+} spin arrangement can change with composition. For ($x>0.5$), the Fe moments on the A and B sites tend to be collinear, whereas for ($x<0.5$), the B-site Fe moments can become noncollinear. This helps explain why changing the Ni/Zn ratio can change (Ms), coercivity, and the overall magnetic state of the composites [12, 25, 47]. A common theme in the literature is the shift from weakly ordered bulk-like behavior to nanoscale superparamagnetic or ferrimagnetic behavior. Bulk $ZnFe_2O_4$ is antiferromagnetic at low temperatures and paramagnetic at higher temperatures, but $ZnFe_2O_4$ nanoparticles often become superparamagnetic because of finite-size effects, surface spin disorder, and cation redistribution. Some nanosized $ZnFe_2O_4$ samples also exhibit room-temperature ferromagnetic behavior, which has been attributed to random Zn/Fe occupation or partial inversion of the spinel sites [12, 32, 35, 40, 48, 51, 53]. For $Zn_{1-x}Ni_xFe_2O_4$, adding Ni generally strengthens the magnetism relative to pure Zn ferrite because magnetic Ni^{2+} replaces the non-magnetic Zn^{2+}. Reviews of $ZnFe_2O_4$ note that Ni doping can enhance magnetization, and direct Ni–Zn ferrite studies report moderate to high (Ms) values depending on the composition and method. Thermally decomposed $Ni_{1-x}Zn_xFe_2O_4$nanoparticles with ($x=0.5–0.7$) showed relatively high saturation magnetization of 71–83 emu/g, while microemulsion- and precipitation-made $Ni_{1-x}Zn_xFe_2O_4$ exhibited similar (Ms) near 45 emu/g but low coercivity [12, 26, 44]. Particle size is one of the most important parameters for magnetic control of particles. In co-precipitated $Zn_{0.3}Ni_{0.7}Fe_2O_4$, the smallest particles showed the onset of superparamagnetic behavior, and the magnetic moment, coercive field, and blocking temperature all changed significantly with the particle size. A similar size dependence appears in pure $ZnFe_2O_4$; one study found room-temperature ferromagnetism for 19–21 nm particles but paramagnetism for larger 29–35 nm particles, and another found superparamagnetic $ZnFe_2O_4$ with blocking temperatures of 18–24

K for 16–22 nm particles [33, 51, 53]. Heat treatment usually increases the magnetization by increasing the crystallinity, particle size, and magnetic ordering of a material. In Zn–Ni ferrite nanoparticles made by coprecipitation, annealing increased the crystallite size from 15.1 to 25.1 nm, increased the coercivity from a soft-magnetic starting point of approximately 45 Oe, and raised the saturation magnetization (Ms) from 11 to 58 emu/g at 800–1000 °C. A similar trend was reported for $Ni_{0.25}Zn_{0.75}Fe_2O_4$ prepared by simple thermal treatment, where calcination from 723 to 873 K increased the particle size from 7 to 25 nm and increased (Ms) from 11 to 26 emu/g. In $ZnFe_2O_4$, the saturation and remanent magnetizations also depend strongly on the particle size and crystallinity [31, 34, 46, 54]. Nanoparticles are often described as soft magnetic materials. Zn–Ni ferrite made by coprecipitation and annealing has low coercivity, and $Ni_{1-x}Zn_xFe_2O_4$ made by microemulsion or precipitation also shows low (Hc) values of approximately 1.3 and 3 kA/m, respectively. $ZnFe_2O_4$ is commonly described as a soft magnetic ferrite with narrow hysteresis loops, low coercivity, and relatively modest saturation magnetization, although the exact values vary significantly with the synthesis route and nanoscale disorder [26, 34, 46]. Another common feature is the blocking behavior of the agents. The solvothermal $Ni_{0.5}Zn_{0.5}Fe_2O_4$ nanospheres were single-domain and superparamagnetic at room temperature, and their blocking temperature increased with synthesis-controlled changes in size and structure. For pure $ZnFe_2O_4$, low-temperature blocking was reported at approximately 18–24 K in co-precipitated nanoparticles, again showing that these ferrites can lie near the superparamagnetic threshold and can be shifted by the synthesis conditions [25, 53]. The synthesis route is important, even when the composition is similar. Manova et al. found that the magnetic properties of $Ni_{1-x}Zn_xFe_2O_4$ particles below 10 nm depend strongly on the phase composition, particle size, and whether the material was synthesized by precipitation plus ball milling or thermal synthesis [45]. Likewise, microemulsion-made and stepwise-precipitated $Ni_{1-x}Zn_xFe_2O_4$ had nearly the same magnetization despite differences in size and strain, showing that route changes do not always strongly change (Ms) but can still alter coercivity, stoichiometry, and microstructure [26]. Taken together, the magnetic properties of $Zn_{1-x}Ni_xFe_2O_4$ nanoparticles can exhibit superparamagnetic, ferrimagnetic, and weak ferromagnetic-like behaviors depending on the synthesis method. In practice, higher annealing or calcination usually increases (Ms), Ni substitution usually strengthens the magnetization compared to pure Zn ferrite, and smaller particles more often exhibit superparamagnetism and size-sensitive blocking. These tunable magnetic responses are the reason why this material is studied for hyperthermia, magnetic fluids, spintronic or memory-related uses, and other high-frequency magnetic applications [25,

33, 34, 43, 44]. Superparamagnetic or weakly coercive Zn–Ni ferrite nanoparticles are attractive for biomedical applications because they respond strongly to external magnetic fields and reduce magnetic agglomeration after the field is removed. Solvothermal $Ni_{0.5}Zn_{0.5}Fe_2O_4$ nanospheres are promising candidates for biomedicine and magnetic fluid technology [25]. Reported biomedical applications of $ZnFe_2O_4$-based nanoparticles include drug delivery/targeting, medical imaging, MRI-related uses, and magnetic resonance imaging, reflecting the same nanoscale magnetic advantage [12, 46, 53]. Nanoparticles have also been proposed as radiosensitizers in cancer therapy, where magnetic nanoparticles can help damage cancer cells under applied fields after radiotherapy [32]. An example of direct Ni–Zn ferrite is magnetic hyperthermia; annealed Zn–Ni ferrite nanoparticles showed an improved specific absorption rate (SAR), and the authors explicitly connected this to hyperthermia applications [34]. $ZnFe_2O_4$ nanoparticles with controlled size and tunable magnetism have also been described as useful for promising biomedical applications [35]. One of the clearest applications of $Zn_{1-x}Ni_xFe_2O_4$ nanoparticles is in magnetic/ferrofluids, because many samples are superparamagnetic at room temperature and have moderate to high saturation magnetization. This use was stated directly for $Ni_{0.5}Zn_{0.5}Fe_2O_4$ nanospheres and also appears in broader zinc ferrite application summaries [25, 40, 46]. Zn–Ni ferrite nanoparticles have also been studied for data storage and memory-related applications because their magnetic state can be tuned by their composition, size, and annealing. The data-storage potential is mentioned in zinc ferrite summaries, and size-tuned $Zn_{0.3}Ni_{0.7}Fe_2O_4$ has been explicitly suggested for spintronics, memory storage, and related device applications [33, 46, 53]. More generally, reviews have noted high-density magnetic information storage and magnetic storage devices as natural targets for ferrite nanoparticles with nanoscale tunable magnetism [12]. Because Ni–Zn ferrites combine soft magnetism with high electrical resistivity and low eddy current loss, they are useful in high-frequency applications, such as rod antennas and inductor/transformer cores. This is a standard application space for Ni–Zn ferrite nanocrystals [31]. $ZnFe_2O_4$-based nanoparticles have also been reported for use in microwave equipment, telecommunication equipment, radio engineering, and radio technology [46, 51]. In addition, zinc ferrite has been actively explored for its microwave absorption properties. A notable example is $ZnFe_2O_4$ quantum dots in carbon-based composites, which exhibit strong reflection-loss performance and useful absorption bandwidths [55]. Zn ferrite nanoparticles are widely used or proposed for catalysis and photocatalysis, and this extends naturally to Ni-doped Zn ferrites because they maintain the ferrite framework while allowing property tuning. These applications have been repeatedly listed in zinc ferrite reviews and studies [40, 41, 46]. A direct Zn–Ni ferrite example

is photocatalytic dye degradation, where size-tuned $Zn_{0.3}Ni_{0.7}Fe_2O_4$ nanoparticles degrade methylene blue, and the smallest particles exhibit the best performance [33]. Zinc ferrite nanoparticles have also been highlighted as adsorbents, water decontaminants, and catalyst supports [40, 41, 56]. Microwave-assisted coprecipitated $ZnFe_2O_4$ with a high surface area has been specifically suggested for catalysis and surface modification [36]. Zinc ferrite nanoparticles are often cited for gas sensor applications, and more general ferrite reviews also place them in a broader category [40, 41, 46]. Beyond magnetic uses, $ZnFe_2O_4$ nanoparticles can also serve as anode materials for Li-ion batteries. This was directly demonstrated for microwave-assisted sol–gel zinc ferrite nanocrystals [42]. Broader zinc ferrite application reviews also list lithium-ion batteries as important research targets [40]. Nickel and zinc nanoparticles have been tested for antimicrobial activity against both Gram-negative and Gram-positive bacteria, with higher Ni/Zn ratio giving stronger activity. The authors suggested its possible use in the hygiene, therapeutic, and textile industries [57]. Ferrite nanoparticle reviews also include antimicrobial agents among the broader application set of spinel ferrites [41]. Zinc ferrites have also been used or proposed as magnetic and optical materials, electronic/semiconductor materials, dielectric materials, and pigments. These applications are broader than those associated with magnetic heating or fluid responses [41, 51, 53].

2.1 Materials

Zinc sulfate ($ZnSO_4H_2O$), nickel chloride ($NiCl_2.4H_2O$), and ferric sulfate ($Fe_2(SO_4)_3.7H_2O$) were used as metal precursors. Ammonia (NH_3) solution was used as the precipitating agent, and polyvinyl alcohol (PVA) was used as the capping agent. All reagents were obtained from Merck.

2. Chemical Co-precipitation Route for $Zn_{1-x}Ni_xFe_2O_4$

The synthesis of $Zn_{1-x}Ni_xFe_2O_4$ ($0.0 < x < 0.04$) nanoparticles through the chemical co-precipitation method involved a meticulously optimized approach to thermodynamics and kinetics, which guaranteed phase purity and precise control over morphology. The process began with the stoichiometric dissolution of metal salt precursors zinc sulfate hydrate, nickel chloride tetrahydrate, and an iron sulfate precursor in 100 mL of deionized water, providing the essential Zn^{2+}, Ni^{2+}, and Fe^{3+} cations required for the mixed-spinel lattice. The crucial phase of precipitation was initiated by introducing a 2 M ammonia (NH_3) solution, which created a highly alkaline environment with a pH of 11[58, 59]. This specific pH, combined with mild

thermal activation at 60 °C and vigorous mechanical agitation at 1000 RPM for 4 h, forces the simultaneous and homogeneous hydrolysis of the metal ions, thereby mitigating localized supersaturation and preventing the sequential formation of secondary impurity phases. To constrain crystallite growth within the nanometer regime and prevent agglomeration driven by high surface energy and van der Waals forces, 1.0 g of polyvinyl alcohol (PVA) was incorporated as a steric capping agent, which passivated the surfaces of the nascent hydroxide nuclei. Following co-precipitation, the precursor material underwent a rigorous two-stage thermal treatment: initial drying at 100 °C for 5 h eliminated volatile solvents and intercalated water, and subsequent high-temperature calcination at 900 °C for 5 h provided the requisite thermodynamic driving forces. This final calcination step combusts the organic PVA polymer and facilitates the complete solid-state transformation of the amorphous mixed hydroxides into the highly ordered, thermodynamically stable cubic spinel ferrite structure, a structural evolution that directly dictates the resulting magnetic parameters of the material, such as the saturation magnetization and specific capacitance.

3. Result and discussion

3.1 Structural Analysis and Phase Evolution

The crystal structure and phase purity of the synthesized $Zn_{1-x}Ni_xFe_2O_4$ ($0.0 < x < 0.04$) nanoparticles were investigated using X-ray diffraction (XRD) [60]. The diffractograms exhibited a significant peak at approximately $2\theta \approx 35°$, corresponding to the (311) crystallographic plane [61]. The indexed peaks corroborated the formation of a cubic structure, consistent with the JCPDS files $ZnFe_2O_4$:22-1012 and NiO:47-1049, as illustrated in Figure 1. Furthermore, the enlarged Figure 2 illustrates the prominent peak (311) shifting towards a lower diffraction angle at 0.01, which increases with the Ni^{2+} concentration, thus resulting in a higher diffraction angle. A shift towards higher diffraction angles is attributed to a smaller (d) spacing, whereas a shift towards lower angles is associated with a larger (d) spacing [62]. The lattice constant (a) was determined using the interplanar spacing (d) of the (311) plane, and as the concentration of Ni^{2+} increased from x = 0.00 to 0.02, the lattice constant decreased systematically from 8.485 Å to 8.451 Å. This lattice contraction is attributed to the substitution of larger Zn^{2+} ions (ionic radius 0.74 Å) with smaller Ni^{2+} ions (ionic radius 0.69 Å) at the interstitial sites [60]. However, an anomalous lattice expansion was observed at x = 0.03, where the lattice constant sharply increased to a maximum of 8.522 Å before relaxing to 8.462 Å at x = 0.04. The average crystallite size (D) and microstrain (ε) were determined using the Scherrer

equation based on the full width at half maximum (FWHM) of the (311) reflection, as shown in Table 2. The measured crystallite sizes ranged from 19.7 to 46.8 nm [63]. In contrast to pure zinc ferrites, nickel ferrites typically possess a reduced activation energy for grain growth. At a calcination temperature of 900 °C, the higher nickel concentration promoted ionic diffusion, which facilitated the merging and increase in individual crystallites [64]. The presence of Ni^{2+} ions alters the coordination strength and chemical bonding energy of the PVA chains. This modification affects the overall stability of the metal-PVA complex, thereby affecting the specific temperature and duration required for crystal formation. Consequently, this leads to an increase in the crystal size from 19.7 to 46.8 nm within the polymer chains [65, 66]. In contrast, the crystallite size pertains to the dimensions of the individual crystalline particles generated during the synthesis. This finding substantiates that the PVA-assisted co-precipitation method effectively restricts particle growth, yielding relatively small crystallites measuring 19.7 nm [66, 67]. Notably, the sample with x = 0.03 exhibited the smallest crystallite size (19.7 nm) and the highest microstrain (0.0058) [39]. This correlation suggests that the anomalous lattice expansion at x = 0.03 is closely linked to an increased density of surface-induced defects and localized lattice distortions, which are anticipated to significantly affect the magnetic and electrochemical properties of the nanoparticles. The sample with x = 0.03 demonstrated these characteristics owing to the anomalous expansion of the lattice at this composition range. This expansion is associated with a high density of surface-induced defects and localized lattice distortions [68]. This correlation indicates that at x = 0.03, the nanoparticles possessed a uniquely high level of structural imperfections on their surface and within the lattice. These defects and distortions alter the physical properties of materials. This phenomenon occurs specifically at the doping concentration or compositional parameter x = 0.03, marking a critical point where the structural and defect characteristics peak, thereby influencing the magnetic and electrochemical properties [69].

3.2 FTIR Analysis

The FTIR spectra of the synthesized $Zn_{1-x}Ni_xFe_2O_4$ (x = 0.00 to 0.04) nanoparticles, recorded in the range of 4000–400 cm^{-1}, confirmed the formation of a cubic spinel structure [70]. As illustrated in Fig. 3, the spectra display two distinct principal absorption bands within the low-frequency range (400–600 cm^{-1}). The higher frequency band (ν_1), observed between 547 and 550 cm^{-1}, is assigned to the intrinsic stretching vibrations of the metal-oxygen (M-O) bonds at the tetrahedral (A) sites [71]. The lower frequency band (ν_2), located between 451 and 460 cm^{-}

^{1}, corresponds to the M-O stretching vibrations at the octahedral (B) site [72]. With increasing Ni^{2+} substitution, the slight shifts observed in the ν_1 and ν_2 band positions were attributed to perturbations in the crystal lattice. Because Ni^{2+} ions have a strong preference for octahedral sites, their introduction forces the partial migration of Fe^{3+} ions from B-sites to the A-sites. This cation redistribution alters the M-O bond lengths, thereby shifting the vibrational frequencies of these bonds [73]. To quantitatively evaluate this structural evolution, the force constants of the tetrahedral (Kt) and octahedral sites (Ko) were determined as follows: The calculated values of Kt (2.19×10^5 to 2.22×10^5 dyne/cm) were systematically higher than those of Ko (1.49×10^5 to 1.55×10^5 dyne/cm) for all samples. This inequality (Kt > Ko) indicates that the A-site M-O bonds are shorter and possess a stronger covalent character than the B-site M-O bonds [74, 75]. In addition to the intrinsic lattice vibrations, a broad band centered around 3358–3417 cm^{-1} and a peak near 1644 $cm^{-1}$are observed, which are assigned to the stretching and bending vibrations of O-H groups from the physically adsorbed water molecules [76]. Furthermore, minor absorption bands in the regions of 2852–2925 cm^{-1}(C-H stretching), ~1741 cm-1(C=O stretching), and 1033–1460 cm^{-1} indicate trace organic residues from the PVA capping agent, while the weak band near 2332–2343 cm^{-1} is characteristic of adsorbed atmospheric CO_2 [77, 78].

3.3 Electrochemical Behavior and Specific Capacitance

The electrochemical properties and electroactive surface area of the synthesized $Zn_{1-x}Ni_xFe_2O_4$ (x = 0.00 to 0.04) nanoparticles were evaluated using cyclic voltammetry (CV) at a constant scan rate of 10 mV/s. Pure zinc ferrite (x = 0.00) exhibited an anodic oxidation peak at 123.3 mV with a peak current of 1.548 μA. Upon the introduction of Ni^{2+} dopants, a profound shift in the redox behavior was observed, and the dominant faradaic reactions transitioned to the cathodic regime, yielding distinct reduction peaks between -146.9 mV and -338.6 mV for the substituted samples [79]. This shift in the electrochemical potential reflects the alteration of the Fermi level and distinct standard reduction potentials of the dynamically redistributed Fe^{3+} and Ni^{2+} cations at the octahedral sites. To quantify the charge storage capability, the specific capacitance (Csp) was calculated from the integrated peak charge area (Q) [80]. The specific capacitance demonstrated a highly concentration-dependent trend, initially dropping at x = 0.01 before surging to maximum values of 6.47 mF/g and 6.24 mF/g for the x = 0.02 and x = 0.03 compositions, respectively. This maximized electrochemical performance perfectly corroborates the nanoparticle size effects determined via XRD [20, 81]. Because the x = 0.03

sample exhibited the smallest crystallite size (19.7 nm) and the highest lattice defect density, it inherently possessed the highest electroactive surface area-to-volume ratio [82]. This expanded solid-liquid interfacial area provides a greater density of active sites for rapid faradaic redox reactions and electrolyte ion intercalation, thereby optimizing the specific capacitance [83, 84]. Beyond this optimal doping threshold (x = 0.04), the crystallite size recovered, the surface-to-volume ratio diminished, and the specific capacitance consequently dropped to 3.14 mF/g. These findings confirm that structural tuning via Ni^{2+} substitution in the x = 0.02–0.03 regime strategically minimizes the nanoparticle size to maximize the electrochemical energy storage potential [12, 25, 31].

3.4 Impedance Analysis and Electrical Transport Properties

Electrochemical impedance spectroscopy (EIS) was conducted to delineate the individual contributions of the grains (bulk) and grain boundaries to the overall electrical transport properties of the $Zn_{1-x}Ni_xFe_2O_4$ (x = 0.00–0.04) nanoparticles [24]. The Nyquist plots (Zim vs. Zre) for all the synthesized compositions exhibited a single depressed semicircle in the high-to-intermediate frequency range. This singular semicircular arc indicates that the electrical conduction is predominantly governed by the grain boundary mechanism rather than the bulk grain mechanism at high temperatures [20]. To extract the quantitative parameters, the Cole-Cole plots were fitted to an equivalent circuit model consisting of a grain resistance (Rg) in series with a parallel combination of a grain boundary resistance (Rgb) and a Constant Phase Element (CPE) [85, 86]. The presence of CPE, evidenced by the depression of the semicircular centers below the real axis (with depression angles θ ranging from 36.75° to 44.73°), indicates a non-ideal Debye-type relaxation behavior. This deviation originates from the inhomogeneous microstructural distribution of grain sizes, lattice defects, and varying cationic site distributions, which are characteristic of nanostructured mixed-spinel structures. The extracted resistance values revealed a profound dependence on the Ni^{2+} substitution concentration of the film [87]. The grain boundary resistance (Rgb) was an order of magnitude higher than the grain resistance (Rg) for all samples, confirming that the grain boundaries act as highly resistive barriers to charge carrier transport [88]. As the Ni^{2+} concentration increased from x = 0.00, Rgb increased significantly, reaching a maximum of 11119.0 Ω at x = 0.03. This impedance maximization corroborates the structural anomalies identified by XRD. The x = 0.03 sample exhibited the minimum crystallite size (19.7 nm) and maximum lattice strain; consequently, it possessed the highest volumetric density of grain boundaries [5, 89]. This dense network of

disordered boundaries, coupled with localized lattice distortions and potential insulating organic residues, severely scatters the charge carriers and restricts electron hopping between Fe^{2+} and Fe^{3+} ions at the octahedral sites, thereby maximizing the macroscopic electrical resistance of the material [20, 24]. Beyond this concentration, at x = 0.04, the crystallite size recovered, the grain boundary volume fraction decreased, and Rgb consequently dropped to 9043.9 Ω. Furthermore, the relaxation parameter (n) approaches a maximum of 0.592 at x=0.03, reflecting a subtle narrowing of the relaxation time distribution as the nanoparticle size becomes highly constrained.

3.5 DLS Analysis and Hydrodynamic Agglomeration Behavior

The hydrodynamic size distribution and colloidal stability of the synthesized $Zn_{1-x}Ni_xFe_2O_4$ (x = 0.00 to 0.04) nanoparticles dispersed in an aqueous medium were evaluated using Dynamic Light Scattering (DLS) [90]. The Cumulants (Z-average) hydrodynamic diameters ranged from 3006.4 nm to 4539.9 nm, while the Contin average diameters extended from 7416.7 nm to 13100.2 nm. These measured hydrodynamic sizes are several orders of magnitude larger than the primary crystallite sizes (19.7–46.8 nm) determined by XRD analysis [18]. This significant dimensional disparity indicates the formation of extensive secondary agglomerates in the aqueous suspension. Macroscopic agglomeration is thermodynamically driven by the inherently high surface-to-volume ratio, intense van der Waals forces, and uncompensated magnetic dipole-dipole interactions characteristic of bare nanoferrites, which dominate the system in the absence of a strong electrostatic or steric stabilizing agent during the aqueous dispersion. The Polydispersity Index (PDI) values further corroborated this colloidal instability [91]. The PDI was exceptionally high for all compositions, ranging from 0.907 to 1.270[17, 18]. A PDI approaching or exceeding 1.0 indicates a highly heterogeneous, polydisperse, and multimodally distributed suspension, confirming severe particle clustering rather than isolated nanoparticles. Notably, the x = 0.03 composition, which exhibited the minimum primary crystallite size (19.7 nm) and maximum defect density in the structural analysis, displayed the largest hydrodynamic agglomerate size (dcumulant = 4539.9 nm) and the highest PDI (1.270) [91–93]. This inverse correlation confirms that the maximized specific surface area of the primary x = 0.03 nanoparticles generated the highest surface free energy, thereby driving the most aggressive macroscopic agglomeration to minimize the thermodynamic instability. Consequently, as dictated by the Stokes-Einstein relationship, the corresponding diffusion

constant concurrently reaches a minimum (1.084×10^{-9} cm^2/s) at this concentration, as the massive clusters experience maximum hydrodynamic drag within the fluid medium [94].

3.6 Morphological Analysis (FE-SEM)

The surface morphology and microstructural architecture of the pure (x = 0.00) and Ni-doped (x = 0.04) Zn-ferrite nanoparticles were examined using field-emission scanning electron microscopy (FE-SEM) at multiple magnification scales (1, 500, 300, and 200 nm). The micrographs revealed that the synthesized particles predominantly exhibited a spherical morphology. The images further display a densely agglomerated particle network, which visually corroborates the extensive secondary clustering and large hydrodynamic diameters previously quantified in the Dynamic Light Scattering (DLS) analysis [95, 96]. This agglomeration is thermodynamically driven by the high surface-to-volume ratio of nanoscale grains and uncompensated magnetic dipole-dipole interactions. Crucially, the high-magnification micrographs revealed a highly porous microstructure distributed throughout the spherical agglomerates for both x = 0.00 and 0.04 [97–100]. The genesis of these numerous pores is a direct consequence of the thermal treatment phase; the high-temperature calcination process drives the rapid evolution of gaseous byproducts, specifically from the dehydration of the precursor hydroxides and complete thermal combustion of the polyvinyl alcohol (PVA) organic capping agent [101–104]. This mesoporous spherical architecture is highly advantageous for the electrochemical performance of the materials. The interconnected porous network mitigates the negative effects of agglomeration by providing pathways for deep electrolyte penetration, thereby increasing the accessible electroactive surface area and directly supporting the charge storage capabilities observed in cyclic voltammetry (CV) analysis [80].

3.7 Magnetic Properties Analysis

The field-dependent magnetization behavior of the annealed $Zn_{1-x}Ni_xFe_2O_4$ ($0.00 \leq x \leq 0.04$) nanoparticles was investigated using Vibrating Sample Magnetometry (VSM) at room temperature. The extracted magnetic parameters revealed a soft ferrimagnetic nature with a strong dependence on both the Ni^{2+} substitution concentration and the associated microstructural evolution. Across all compositions, the remanence ratio (R = Mr/Ms) was confined to exceptionally low values, ranging from 0.0033 to 0.0529. Because these values are significantly less than the theoretical limit of 0.5 for randomly oriented non-interacting particles, this indicates that the nanoferrites possess a multi-domain structure or exhibit near-

superparamagnetic relaxation at RT [34, 44, 105]. The saturation magnetization (Ms) and calculated net magnetic moment (μB) displayed a nonlinear trend, characterized by a sharp decline at the critical doping concentration of x = 0.03 (Ms = 23.087 $\times 10^{-3}$ emu/g). This sudden suppression of magnetization corroborates the structural anomalies previously identified via X-ray diffraction. The x = 0.03 sample exhibited the absolute minimum primary crystallite size (19.7 nm) and maximized lattice microstrain [5, 106]. In such deep nanoscale regimes, the surface-to-volume ratio is maximized, giving rise to a prominent magnetically "dead" surface layer that is not magnetized. Within this disordered boundary layer, broken exchange bonds and severe spin canting neutralize the A-B sublattice superexchange interactions, thereby suppressing the net macroscopic magnetization [107, 108]. Conversely, the coercivity (Hc) and effective magnetocrystalline anisotropy constant (K) demonstrated a massive surge at this same concentration, reaching 150.0 Oe and 1.732 erg/g, respectively, at x = 0.03. This pronounced magnetic hardening is a direct consequence of the maximized defect density and dense grain boundary network [5, 89, 109]. Localized lattice distortions and extensive surface defects act as potent pinning centers that restrict the rotation of magnetic spins and impede domain wall motion. Ultimately, these VSM findings confirm that the microstructural size reduction and strain maximization achieved at x = 0.03 not only optimize the electroactive surface area for capacitance but also fundamentally alter the superexchange interactions and anisotropy of the Zn ferrite lattice [5, 8, 9].

4. Conclusions

This study explores how small amounts of Ni^{2+} substitution ($0.0 < x < 0.04$) affect the defect engineering of $Zn_{1-x}Ni_xFe_2O_4$ spinel nanoparticles. It links changes in the structure to the magnetic and electrochemical properties of the nanoparticles. Spinel ferrites are known for their sensitivity to the distribution of cations between tetrahedral (A) and octahedral (B) sites. Additionally, nanoparticles can cause $ZnFe_2O_4$ to deviate from antiferromagnetism owing to surface effects and Fe^{3+} redistribution. XRD analysis confirmed the formation of a cubic spinel structure in the studied compositions. It showed lattice contraction from a = 8.485 Å (x = 0.00) to 8.451 Å (x = 0.02) as larger Zn^{2+} (0.74 Å) was replaced by smaller Ni^{2+} (0.69 Å), followed by an anomaly at x = 0.03 (a = 8.522 Å) and relaxation at x = 0.04 (8.462 Å). The crystallite sizes spanned 19.7–46.8 nm; x = 0.03 showed the minimum size (19.7 nm) and maximum microstrain (0.0058). FTIR analysis corroborated spinel formation via bands (ν1 = 547–550 cm^{-1} for A-site and ν2 = 451–460 cm^{-1} for B-site M–O vibrations), with force constants Kt >

Ko (2.19–2.22×10^5 vs. 1.49–1.55×10^5 dyne/cm) and contributions from adsorbed water (~3358–3417 and 1644 cm^{-1}), atmospheric CO_2 (~2332–2343 cm^{-1}), and PVA residues (C–H 2852–2925 cm^{-1}; C=O ~1741 cm^{-1}; 1033–1460 cm^{-1}). EIS showed plots with depressed semicircles dominated by grain boundaries. Fitting to an Rg–(Rgb‖CPE) model indicated non-Debye relaxation (θ = 36.75°–44.73°, n up to 0.592) and dependence, with Rgb (≫Rg) peaking at 11119.0 Ω at x = 0.03 and 9043.9 Ω at x = 0.04. Despite nanometric primary crystallites, colloidal measurements revealed severe aqueous agglomeration: DLS Z-average diameters of 3006.4–4539.9 nm (Contin average 7416.7–13100.2 nm) with high PDI (0.907–1.270), worst at x = 0.03, where diffusion reached a minimum (1.084×10^{-9} cm^2/s), indicating that surface free energy and magnetic dipolar interactions drive secondary clustering. FE-SEM confirmed agglomerated spherical assemblies with mesoporosity from dehydration and PVA combustion, providing electrolyte-accessible pathways during the operation. Cyclic voltammetry (10 mV s^{-1}) showed that pure $ZnFe_2O_4$ had an anodic peak at 123.3 mV, whereas Ni substitution shifted the behavior to cathodic reduction peaks (−146.9 to −338.6 mV), reflecting redox energetics with cation redistribution. The specific capacitance decreased at x = 0.01, peaked at x = 0.02–0.03, and then declined at x = 0.04. Room-temperature VSM indicated soft ferrimagnetic/near-superparamagnetic behavior (Mr/Ms = 0.0033–0.0529), but critical hardening at x = 0.03, where Ms sharply decreased to 23.087×10^{-3} emu g^{-1}, while coercivity and anisotropy surged (Hc = 150.0 Oe; K = 1.732 erg g^{-1}), consistent with enhanced surface “dead-layer” spin canting and grain-boundary/defect pinning. A narrow compositional threshold of approximately x = 0.03 maximizes the defect density and grain-boundary networks, simultaneously increasing the coercivity and optimizing faradaic charge storage. This demonstrates that controlled low-level Ni doping effectively co-tunes the magnetic functionality and electrochemical energy storage performance of Zn ferrite nanomaterials.

Acknowledgments:

The authors gratefully acknowledge the St. Joseph's College of Arts and Science (Autonomous), Cuddalore, Tamil Nadu, India, for their invaluable provision of laboratory (NCR) and library access, which was crucial for the successful completion of this research.

Funding:

This research did not receive any specific grant from funding agencies in the public, commercial, or not-for-profit sectors

Data Availability:

The datasets generated and analysed during the current study are available from the corresponding author upon reasonable request

References

1. Hossain, M.F., Awal, M.A., Islam, M.J., Khatun, M.T., Islam, S., Jellur Rahman, M.: Synthesis and characterization of structural, magnetic and electrical properties of Mn substituted Co-Zn ferrite. Journal of Magnetism and Magnetic Materials. 588, 171440 (2023). https://doi.org/10.1016/j.jmmm.2023.171440

2. Mandal, D., Alam, M., Mandal, K.: $NiFe_2O_4$ nano-hollow spheres with improved magnetic and dielectric properties. Physica B: Condensed Matter. 554, 51–56 (2018). https://doi.org/10.1016/j.physb.2018.11.008

3. Sanchez-Lievanos, K.R., Stair, J.L., Knowles, K.E.: Cation Distribution in Spinel Ferrite Nanocrystals: Characterization, Impact on their Physical Properties, and Opportunities for Synthetic Control. Inorg. Chem. 60, 4291–4305 (2021). https://doi.org/10.1021/acs.inorgchem.1c00040

4. Sagayaraj, R., Aravazhi, S., Chandrasekaran, G.: Review on structural and magnetic properties of (Co–Zn) ferrite nanoparticles. Int Nano Lett. 11, 307–319 (2021). https://doi.org/10.1007/s40089-021-00343-z

5. Swain, M., Dash, C.A., Parija, D., Ray, J., Badapanda, T.: Study of structural and magnetic behavior of Zn doped spinel nickel ferrites ($Ni_{1-x}Zn_xFe_2O_4$). In: AIP conference proceedings. p. 020194. Cornell University (2024)

6. Mazen, S., Abu-Elsaad, N.I., Nawara, A.S.: The Influence of Various Divalent Metal Ions (Mn^{2+}, Co^{2+}, and Cu^{2+}) Substitution on the Structural and Magnetic Properties of Nickel–Zinc Spinel Ferrite. Phys. Solid State. 62, 1183–1194 (2020). https://doi.org/10.1134/s106378342007015x

7. Ansari, M.R., Sen, S., Jayasimhadri, M., Peta, K.R.: Exploring Properties of Spinel-Structured Co-Doped $ZnFe_2O_4$ for Hydrogen and Oxygen Evolution and Supercapacitor Applications. Energy Tech. 14, (2026). https://doi.org/10.1002/ente.202502559

8. Zviagin, V., Grundmann, M., Schmidt-Grund, R.: Impact of Defects on Magnetic Properties of Spinel Zinc Ferrite Thin Films. Physica Status Solidi (b). 257, 1900630 (2020). https://doi.org/10.1002/pssb.201900630

9. Yuan, Q., Pan, L., Liu, R., Wang, J., Liao, Z., Qin, L., Bi, J., Gao, D., Wu, J.: Cation Distribution and Magnetism in Quenched $ZnFe_2O_4$. Journal of Elec Materi. 47, 3608–3614 (2018). https://doi.org/10.1007/s11664-018-6206-9

10. Kmita, A., Żukrowski, J., Kuciakowski, J., Marciszko-Wiąckowska, M., Żywczak, A., Lachowicz, D., Gajewska, M., Sikora, M.: Effect of Thermal Treatment at Inert Atmosphere on Structural and Magnetic Properties of Non-stoichiometric Zinc Ferrite Nanoparticles. Metall Mater Trans A. 52, 1632–1648 (2021). https://doi.org/10.1007/s11661-021-06154-3

11. Bini, M., Ambrosetti, M., Spada, D.: $ZnFe_2O_4$, a Green and High-Capacity Anode Material for Lithium-Ion Batteries: A Review. Applied Sciences. 11, 11713 (2021). https://doi.org/10.3390/app112411713

12. Bhattu, M., Acevedo, R., Shnain, A.H.: A comprehensive review on the synthesis routes, properties and potential applications of $ZnFe_2O_4$ ferrites. E3S Web Conf. 588, 02014 (2024). https://doi.org/10.1051/e3sconf/202458802014

13. Ambrosetti, M., Spada, D., Mozzati, M.C., Albini, B., Galinetto, P., Cini, A., Fittipaldi, M., Bini, M.: Physico-Chemical and Electrochemical Features of Nanometric $ZnFe_2O_4$, Anode Material for Libs. Meet. Abstr. MA2022-01, 2249 (2022). https://doi.org/10.1149/ma2022-01552249mtgabs

14. Hejazi, A.S., Al-Hunaiti, A.H., Bsoul, I., Mohaidat, Q., Mahmood, S.H.: Optimizing the synthesis of $ZnFe_2O_4$ through chemical and physical methods: effects of the synthesis route on the phase purity, inversion, and magnetic properties of spinel zinc ferrite. Phys. Scr. 99, 065029 (2024). https://doi.org/10.1088/1402-4896/ad4746

15. Soni, H., Acevedo, R., Obad, S., Kumar, B.: Structural, Magnetic, and Catalytic traits of Nickel Ferrite: A review. E3S Web Conf. 588, 02012 (2024). https://doi.org/10.1051/e3sconf/202458802012

16. Kamzin, A.S., Bingolbali, A., Doğan, N., Yeşil, Z., Asiltürk, M.: The Magnetic Structure of $NiFe_2O_4$ Nanoparticles. Tech. Phys. Lett. 45, 1008–1011 (2019). https://doi.org/10.1134/s1063785019100092

17. Sankari, S.M., Sagayayaraj, R., Sebastian, S., Amalorpavadoss, A., Porkalai, V., Aravazhi, S., Chandrasekaran, G.: Enhanced Magnetic Softness and Specific Capacitance in $Mg_{0.5}Zn_{0.5}Fe_2O_4$ Nanoferrites, (2026)

18. Xavier, I.D., Sagayaraj, R., Sebastian, S., Aravazhi, S.: Synthesis and Characterization of Mn-Substituted $ZnFe_2O_4$ Nanoparticles: Probing the Influence of Mn Content on Microstructure and Magnetic Properties. Chemistry Africa. 9, (2026). https://doi.org/10.1007/s42250-026-01656-2

19. Lyla, P.: Structural And Magnetic Properties Of Spinel Mg-Ni Ferrites Nanoparticles Synthesized By Microwave Combustion Method. Turkish Journal of Computer and Mathematics Education (TURCOMAT). 12, 1455–1461 (2021). https://doi.org/10.17762/turcomat.v12i10.4466

20. Raj, R.S.A., Joseph, A., Suresh, S., Joy, L.K.: $Zn_{1-x}Ni_x Fe_2O_4$ Electrodes for Symmetric Supercapacitors: Sustained Electrochemical Stability With Multiple Charge Storage Pathways. Advanced Sustainable Systems. 10, (2026). https://doi.org/10.1002/adsu.202501282

21. Ciocarlan, R.-G., Seftel, E.M., Gavrila, R., Suchea, M., Batuk, M., Mertens, M., Hadermann, J., Cool, P.: Spinel nanoparticles on stick-like Freudenbergite nanocomposites as effective smart-removal photocatalysts for the degradation of organic pollutants under visible light. Journal of Alloys and Compounds. 820, 153403 (2019). https://doi.org/10.1016/j.jallcom.2019.153403

22. Zhu, X., Wei, Z., Zhao, W., Zhang, X.-D., Wu, X.-J., Jiang, J.-L.: Preparation and Characterization of $Zn_{1-x}Ni_xFe_2O_4$ Nanoparticles with Spinel Structure Synthesized by Hydrothermal Method. CNANO. 14, 474–480 (2018). https://doi.org/10.2174/1573413714666180528074117

23. Zito, C.A., Orlandi, M.O., Volanti, D.P.: Accelerated microwave-assisted hydrothermal/solvothermal processing: Fundamentals, morphologies, and applications. J Electroceram. 40, 271–292 (2018). https://doi.org/10.1007/s10832-018-0128-z

24. Atif, M., Nadeem, M.: Sol–gel synthesis of nanocrystalline $Zn_{1-x}Ni_xFe_2O_4$ ceramics and its structural, magnetic and dielectric properties. J Sol-Gel Sci Technol. 72, 615–626 (2014). https://doi.org/10.1007/s10971-014-3484-4

25. Liu, R., Yu, Q., Liu, Y., Liu, X., Wang, F., Xu, Y.: Optimization of Citrate-Gel Preparation Process for Magnetic Ni-Zn Ferrite Nanoparticles. j nanosci nanotechnol. 18, 2838–2843 (2018). https://doi.org/10.1166/jnn.2018.14308

26. Plutenko, T., V'Yunov, O., Fedorchuk, O., Solopan, S., Plutenko, M., Khomenko, B.: MICROEMULSION-BASED METHOD OF SYNTHESIS OF ZINC-NICKEL FERRITE AND THEIR MAGNETIC PROPERTIES. Ukr. Chem. Journ. 88, 16–28 (2022). https://doi.org/10.33609/2708-129x.88.07.2022.16-28

27. Mouallem-Bahout, M., Bertrand, S., Peña, O.: Synthesis and characterization of $Zn_{1-x}Ni_xFe_2O_4$ spinels prepared by a citrate precursor. Journal of Solid State Chemistry. 178, 1080–1086 (2005). https://doi.org/10.1016/j.jssc.2005.01.009

28. Azouzi, W., Boulahya, I., Robert, J., Essyed, A., Mahmoud, A., Al Shami, A., Ihiawakrim, D., Labrim, H., Benaissa, M.: Ultrasonic chemical synthesis of zinc-manganese ferrites with improved magnetic properties. Ultrasonics Sonochemistry. 111, 107108 (2024). https://doi.org/10.1016/j.ultsonch.2024.107108

29. Velinov, N., Manova, E., Tsoncheva, T., Estournès, C., Paneva, D., Tenchev, K., Petkova, V., Koleva, K., Kunev, B., Mitov, I.: Spark plasma sintering synthesis of $Ni_{1-x}Zn_xFe_2O_4$ ferrites: Mössbauer and catalytic study. Solid State Sciences. 14, 1092–1099 (2012). https://doi.org/10.1016/j.solidstatesciences.2012.05.023

30. Maalam, K.E., Fkhar, L., Hamedoun, M., Mahmoud, A., Boschini, F., Hlil, E.K., Benyoussef, A., Mounkachi, O.: Magnetocaloric Properties of Zinc-Nickel Ferrites Around Room Temperature. J Supercond Nov Magn. 30, 1943–1947 (2017). https://doi.org/10.1007/s10948-016-3961-9

31. Leng, P.L., Naseri, M.G., Saion, E., Shaari, A.H., Kamaruddin, M.A.: Synthesis and Characterization of Ni-Zn Ferrite Nanoparticles by Thermal Treatment Method. ANP. 02, 378–383 (2013). https://doi.org/10.4236/anp.2013.24052

32. Sari, R.S., Hakim, A.R.: Bonding analysis of magnetic nanoparticles (MNPS) zinc ferrite ($ZnFe_2O_4$) encapsulated with silica (SIO2). IOP Conf. Ser.: Earth Environ. Sci. 382, 012019 (2019). https://doi.org/10.1088/1755-1315/382/1/012019

33. Mondal, N.J., Sonkar, R., Boro, B., Ghosh, M.P., Chowdhury, D.: Nanocrystalline Ni-Zn spinel ferrites: size-dependent physical, photocatalytic and antioxidant properties. Nanoscale Adv. 5, 5460–5475 (2023). https://doi.org/10.1039/d3na00446e

34. Suharyadi, E., Pratiwi, S.H., Indrayana, I.P.T., Kato, T., Iwata, S., Ohto, K.: Effects of annealing temperature on microstructural, magnetic properties, and specific absorption rate of Zn-Ni ferrite nanoparticles. Mater. Res. Express. 8, 036101 (2021). https://doi.org/10.1088/2053-1591/abe986

35. Sagayaraj, R., Aravazhi, S., Praveen, P., Chandrasekaran, G.: Structural, morphological and magnetic characters of PVP coated $ZnFe_2O_4$ nanoparticles. J Mater Sci: Mater Electron. 29, 2151–2158 (2017). https://doi.org/10.1007/s10854-017-8127-4

36. Ochmann, M., Vrba, V., Kopp, J., Ingr, T., Malina, O., Machala, L.: Microwave-Enhanced Crystalline Properties of Zinc Ferrite Nanoparticles. Nanomaterials. 12, 2987 (2022). https://doi.org/10.3390/nano12172987

37. Kumari, H., Sharma, S., Kumar, A., Parmar, R., Rani, P., Godara, P., Singh, R.M., Jain, R., Asha, A.: Structural, magnetic, and photocatalytic properties of Ce^{3+} ion doped Ni Zn ferrite nanoparticles. Journal of Magnetism and Magnetic Materials. 636, 173671 (2025). https://doi.org/10.1016/j.jmmm.2025.173671

38. Ilosvai, Á.M., Forgách, L., Kovács, N., Heydari, F., Szigeti, K., Máthé, D., Kristály, F., Daróczi, L., Kaleta, Z., Viskolcz, B., Nagy, M., Vanyorek, L.: Development of Polymer-Encapsulated, Amine-Functionalized Zinc Ferrite Nanoparticles as MRI Contrast Agents. IJMS. 24, 16203 (2023). https://doi.org/10.3390/ijms242216203

39. Shunmuga Sundaram, P., Sangeetha, T., Rajakarthihan, S., Vijayalaksmi, R., Elangovan, A., Arivazhagan, G.: XRD structural studies on cobalt doped zinc oxide nanoparticles synthesized by coprecipitation method: Williamson-Hall and size-strain plot approaches. Physica B: Condensed Matter. 595, 412342 (2020). https://doi.org/10.1016/j.physb.2020.412342

40. Shaterian, M., Rezvani, A., Abbasian, A.R.: Controlled synthesis and self-assembly of $ZnFe_2O_4$ nanoparticles into microspheres by solvothermal method. Mater. Res. Express. 6, 1250e5 (2019). https://doi.org/10.1088/2053-1591/ab65e0

41. Dippong, T., Levei, E.A., Cadar, O.: Recent Advances in Synthesis and Applications of MFe_2O_4 (M = Co, Cu, Mn, Ni, Zn) Nanoparticles. Nanomaterials. 11, 1560 (2021). https://doi.org/10.3390/nano11061560

42. Suchomski, C., Breitung, B., Witte, R., Knapp, M., Bauer, S., Baumbach, T., Reitz, C., Brezesinski, T.: Microwave synthesis of high-quality and uniform 4 nm $ZnFe_2O_4$ nanocrystals for application in energy storage and nanomagnetics. Beilstein J. Nanotechnol. 7, 1350–1360 (2016). https://doi.org/10.3762/bjnano.7.126

43. Khalafallah, A.Y., Siddig, M.A., Algethami, O.A., Elbadawi, A.A., Mohammed, A.S.: Influence of preparation method on structural, optical and magnetic properties of synthesized $Zn_{0.5}Mg_{0.5-x}Ni_xFe_2O_4$ nano-ferrite. Mater. Res. Express. 11, 055003 (2024). https://doi.org/10.1088/2053-1591/ad477d

44. Hwang, J., Choi, M., Shin, H.-S., Ju, B.-K., Chun, M.: Structural and Magnetic Properties of NiZn Ferrite Nanoparticles Synthesized by a Thermal Decomposition Method. Applied Sciences. 10, 6279 (2020). https://doi.org/10.3390/app10186279

45. Manova, E., Paneva, D., Kunev, B., Rivière, E., Estournès, C., Mitov, I.: Characterization of nanodimensional Ni-Zn ferrite prepared by mechanochemical and thermal methods. J. Phys.: Conf. Ser. 217, 012102 (2010). https://doi.org/10.1088/1742-6596/217/1/012102

46. Sunandar, M., Tiana, S., Yunasfi, Y.: Phase analysis and magnet properties of $Zn_xFe_{(3-x)}O_4$ prepared by milling process. Mal. J. Fund. Appl. Sci. 14, 208–212 (2018). https://doi.org/10.11113/mjfas.v14n2.940

47. Hasan, S., Azhdar, B.: Synthesis of Nickel-Zinc Ferrite Nanoparticles by the Sol-Gel Auto-Combustion Method: Study of Crystal Structural, Cation Distribution, and Magnetic Properties. Advances in Condensed Matter Physics. 2022, 1–14 (2022). https://doi.org/10.1155/2022/4603855

48. Berhanu, H., Raghavender, A., Kebede, L., Anjaneyulu, T.: Ferromagnetic Behavior in Zinc Ferrite Nanoparticles Synthesized using Coprecipitation Technique. Sci. Technol. Arts Res. J. 3, 85 (2015). https://doi.org/10.4314/star.v3i4.12

49. Pratibha, G., Thirupathi, A., Vamsi Krishna, V.K., Siva Kumar, P., Siva Sankara Yadav, G.K.: Effect of Ni substitution on structural, dielectric and magnetic properties of Zn ferrite nanoparticles. JOR. 17, 323–331 (2021). https://doi.org/10.15251/jor.2021.174.323

50. Velmurugan, K., Venkatachalapathy, V.S.K., Sendhilnathan, S.: Synthesis of nickel zinc iron nanoparticles by coprecipitation technique. Mat. Res. 13, 299–303 (2010). https://doi.org/10.1590/s1516-14392010000300005

51. Anjaneyulu, T., Raghavender, A., Vijaya Kumar, K., Narayana Murthy, P., Narendra, K.: Effect of Particle Size on the Structural and Magnetic Properties of Nanocrystalline Zinc Ferrite. Sci. Technol. Arts Res. J. 3, 48 (2014). https://doi.org/10.4314/star.v3i3.8

52. Puspitasari, P., Rizkia, U.A., Sukarni, S., Permanasari, A.A., Taufiq, A., Putra, A.B.N.R.: Effects of Various Sintering Conditions on the Structural and Magnetic Properties of Zinc Ferrite ($ZnFe_2O_4$). Mat. Res. 24, (2021). https://doi.org/10.1590/1980-5373-mr-2020-0300

53. Maalam, K.E., Fkhar, L., Mahhouti, Z., Mounkachi, O., Aitali, M., Hamedoun, M., Benyoussef, A.: The effects of synthesis conditions on the magnetic properties of zinc ferrite spinel nanoparticles. J. Phys.: Conf. Ser. 758, 012008 (2016). https://doi.org/10.1088/1742-6596/758/1/012008

54. Sajjan, S., Kulkarni, A., Gounhalli, S.G.: Influence of Zirconium substitution on electrical properties of Nickel-Zinc Ferrites. IOP Conf. Ser.: Mater. Sci. Eng. 1300, 012032 (2024). https://doi.org/10.1088/1757-899x/1300/1/012032

55. Gao, Z., Xu, B., Ma, M., Feng, A., Zhang, Y., Liu, X., Jia, Z., Wu, G.: Electrostatic self-assembly synthesis of $ZnFe_2O_4$ quantum dots ($ZnFe_2O_4$@C) and electromagnetic microwave

absorption. Composites Part B: Engineering. 179, 107417 (2019). https://doi.org/10.1016/j.compositesb.2019.107417

56. Kaedi, F., Yavari, Z., Asmaei, M., Abbasian, A.R., Noroozifar, M.: Ethanol electrooxidation on high-performance mesoporous $ZnFe_2O_4$-supported palladium nanoparticles. New J. Chem. 43, 3884–3890 (2019). https://doi.org/10.1039/c8nj05950k

57. Liaqat, I., Shaanzeh, Z., Bibi, A., Zafar, U., Naseem, S., Ali, R., Andleeb, S., Saleem, G., Liaqat, I., Afzaal, M.: In vitro Antimicrobial Activity of Biogenically Synthesized Nickel and Zinc Nanoparticles against Selected Pathogenic Bacterial Strains. J. Oleo Sci. 71, 1181–1188 (2022). https://doi.org/10.5650/jos.ess22068

58. Sagayaraj, R., Sebastian, S.: Improved optical and magnetic properties of polycrystalline Z-type hexaferrites by co-precipitation method. Appl. Phys. A. 129, (2023). https://doi.org/10.1007/s00339-022-06370-7

59. Poongodi, R., Senguttuvan, S., Sebastian, S., Sagayaraj, R.: Analyzing the variations in electrical, structural and magnetic properties of zinc-doped $MnFe_2O_4$ ferrite obtained via co-precipitation. J Aust Ceram Soc. 60, 1483–1494 (2024). https://doi.org/10.1007/s41779-024-01057-z

60. Abu El-Fadl, A., Hassan, A.M., Mahmoud, M.H., Tatarchuk, T., Yaremiy, I.P., Gismelssed, A.M., Ahmed, M.A.: Synthesis and magnetic properties of spinel $Zn_{1-x}Ni_xFe_2O_4$ ($0.0 \leq x \leq 1.0$) nanoparticles synthesized by microwave combustion method. Journal of Magnetism and Magnetic Materials. 471, 192–199 (2018). https://doi.org/10.1016/j.jmmm.2018.09.074

61. Sagayaraj, R., Aravazhi, S., Selva Kumar, C., Senthil Kumar, S., Chandrasekaran, G.: Tuning of ferrites ($Co_xFe_{3-x}O_4$) nanoparticles by co-precipitation technique. SN Appl. Sci. 1, (2019). https://doi.org/10.1007/s42452-019-0244-7

62. Vinosha, P.A., Vinsla, J.V.A., Madhavan, J., Devanesan, S., Alsalhi, M.S., Nicoletti, M., Xavier, B.: Impact of dysprosium doped (Dy) zinc ferrite ($ZnFe_2O_4$) nanocrystals in photo-fenton exclusion of recalcitrant organic pollutant. Environmental Research. 203, 111913 (2021). https://doi.org/10.1016/j.envres.2021.111913

63. Poongodi, R., Senguttuvan, S., Sagayaraj, R.: Exploring the Decreasing Coercivity Properties of Aluminum Cobalt Ferrites Prepared by Coprecipitation Method. ajc. 35, 1781–1787 (2023). https://doi.org/10.14233/ajchem.2023.27807

64. Tsega, M.: Structural and optical properties of Mn-doped anatase-rutile TiO_2 nanoparticles. Indian J Phys. 99, 177–189 (2024). https://doi.org/10.1007/s12648-024-03275-4

65. Pydiraju, T.R.K., H Rao, K., Appa Rao, P., Chaitanya Varma, M., Satish Kumar, A., Srinivasa Rao, K.: Co-Cd nanoferrite for high frequency application with phenomenal rise in DC resistivity. Journal of Magnetism and Magnetic Materials. 524, 167662 (2020). https://doi.org/10.1016/j.jmmm.2020.167662

66. Ortiz-Quiñonez, J.-L., Pal, U., Villanueva, M.S.: Structural, Magnetic, and Catalytic Evaluation of Spinel Co, Ni, and Co–Ni Ferrite Nanoparticles Fabricated byLow-Temperature Solution Combustion Process. ACS Omega. 3, 14986–15001 (2018). https://doi.org/10.1021/acsomega.8b02229

67. Andhare, D.D., Patade, S.R., Kounsalye, J.S., Jadhav, K.M.: Effect of Zn doping on structural, magnetic and optical properties of cobalt ferrite nanoparticles synthesized via. Co-precipitation method. Physica B: Condensed Matter. 583, 412051 (2020). https://doi.org/10.1016/j.physb.2020.412051

68. Almessiere, M.A., Slimani, Y., Güngüneş, H., Korkmaz, A.D., Zubar, T., Trukhanov, S., Trukhanov, A., Manikandan, A., Alahmari, F., Baykal, A.: Influence of Dy^{3+} Ions on the Microstructuresand Magnetic, Electrical, and Microwave Properties of Spinel Ferrites. ACS Omega. 6, 10266–10280 (2021). https://doi.org/10.1021/acsomega.1c00611

69. Karthik, K., Selvan, G.K., Kanagaraj, M., Arumugam, S., Jaya, N.V.: Particle size effect on the magnetic properties of NiO nanoparticles prepared by a precipitation method. Journal of Alloys and Compounds. 509, 181–184 (2010). https://doi.org/10.1016/j.jallcom.2010.09.033

70. Srinivas, C., Deepty, M., Kumar, E.R., Prasad, S.A.V., Tirupanyam, B.V., Meena, S.S., Prajapat, C.L., Sastry, D.L.: Rietveld refinement and FTIR spectroscopic studies of Ni^{2+}-substituted Zn-ferrite nanoparticles. Appl. Phys. A. 125, (2019). https://doi.org/10.1007/s00339-019-2840-1

71. Almutairi, T.S.: Unraveling the Complex Interplay of Phase Transitions in Spinel Ferrites: A Comprehensive Quantum Mechanical Vibrational Study of $ZnFe_2O_4$. ACS Omega. 8, 36999–37010 (2023). https://doi.org/10.1021/acsomega.3c04268

72. Abdelhakim, N.A., Hemeda, O.M., Shalaby, R.M., Mostafa, M.: The role of phase transformation (tetragonal – spinel) on the structural and mechanical properties of Ni doped $CuFe_2O_4$. Appl. Phys. A. 130, (2024). https://doi.org/10.1007/s00339-024-07808-w

73. Boussafel, H., Sedrati, C., Alleg, S., Zine, A., Frégnaux, M., Tambosi, R., Kebaili, N.: Structural, properties and compositional modifications in non-stoichiometric Ni-substituted cobalt ferrites. Appl. Phys. A. 131, (2025). https://doi.org/10.1007/s00339-025-08894-0

74. Patil, B.B., Pawar, A.D., Bhosale, D.B., Ghodake, J.S., Thorat, J.B., Shinde, T.J.: Effect of La^{3+} substitution on structural and magnetic parameters of Ni–Cu–Zn nano-ferrites. J Nanostruct Chem. 9, 119–128 (2019). https://doi.org/10.1007/s40097-019-0302-0

75. El-Said Bakeer, D., El Sayed, M.Y., Abdallah, E.M., Awad, R., Elsharkawy, S.G.: Structural and magnetic tailoring of Co-Cu ferrite nanoparticles via Cd^{2+} substitution: a multi-characterization approach. Appl. Phys. A. 131, (2025). https://doi.org/10.1007/s00339-025-08897-x

76. Al-Soihi, A.S., Alsulami, Q.A., Mostafa, M.M.M.: Amalgamated Titanium Oxide-Carbon Hollow Sphere/Nickel-Layered Double Hydroxide as an Efficient Photocatalyst for the Degradation of Methyl Orange. Catalysts. 12, 1200 (2022). https://doi.org/10.3390/catal12101200

77. Vartanyan, M., Voytovich, I., Gorbunova, I., Makarov, N.: Preparation and Structural Characterization of Complex Oxide Eutectic Precursors from Polymer–Salt Xerogels Obtained by Microwave-Assisted Drying. Materials. 13, 1808 (2020). https://doi.org/10.3390/ma13081808

78. Alijani, S., Capelli, S., Cattaneo, S., Schiavoni, M., Evangelisti, C., Mohammed, K.M.H., Wells, P.P., Tessore, F., Villa, A.: Capping Agent Effect on Pd-Supported Nanoparticles in the Hydrogenation of Furfural. Catalysts. 10, 11 (2019). https://doi.org/10.3390/catal10010011

79. Jyothish, B., Jacob, J.: Synthesis and characterization of Ni^{2+} and Al^{3+} doped zinc ferrite nanoparticles for antibacterial, antioxidant, and anticancer (MCF-7) analysis. Chemical Physics Impact. 6, 100209 (2023). https://doi.org/10.1016/j.chphi.2023.100209

80. Li, L., Jin, G., Shen, J., Guo, M., Song, J., Li, Y., Xiong, J.: Carbon Aerogels: Synthesis, Modification, and Multifunctional Applications. Gels. 11, 548 (2025). https://doi.org/10.3390/gels11070548

81. Yeasmin, S., Jain, A., Sobczak, K., Sarmah, K., Dobrotvorska, M.V., Lewandowski, M., Mahanta, D.: A Facile In Situ Template Method to Fabricate Hollow Polypyrrole Nanoparticles for Asymmetric Electrochemical Capacitors with Enhanced Cyclic Stability. ChemSusChem. 18, e202501334 (2025). https://doi.org/10.1002/cssc.202501334

82. Wang, R., Lang, J., Liu, Y., Lin, Z., Yan, X.: Ultra-small, size-controlled Ni $(OH)_2$ nanoparticles: elucidating the relationship between particle size and electrochemical performance for advanced energy storage devices. NPG Asia Mater. 7, e183 (2015). https://doi.org/10.1038/am.2015.42

83. Yang, N., Yu, S., Zhang, W., Cheng, H., Simon, P., Jiang, X.: Electrochemical Capacitors with Confined Redox Electrolytes and Porous Electrodes. Advanced Materials. 34, 2202380 (2022). https://doi.org/10.1002/adma.202202380

84. Azmi, S., Frackowiak, E.: Redox activity from the electrolyte and electrode in electrochemical capacitors. Electrochemistry Communications. 138, 107289 (2022). https://doi.org/10.1016/j.elecom.2022.107289

85. Simić, M., Jeoti, V., Stojanović, G.M.: Parameter extraction of the Cole-impedance model for in-situ monitoring of electrochemical sources. Journal of Energy Storage. 77, 109895 (2023). https://doi.org/10.1016/j.est.2023.109895

86. Jorcin, J.-B., Orazem, M.E., Pébère, N., Tribollet, B.: CPE analysis by local electrochemical impedance spectroscopy. Electrochimica Acta. 51, 1473–1479 (2005). https://doi.org/10.1016/j.electacta.2005.02.128

87. Devi, E.C., Soibam, I.: Structural and electrical studies of Mn-Ni mixed nanoferrites. IJNP. 9, 120 (2017). https://doi.org/10.1504/ijnp.2017.10007143

88. Magar, H.S., Hassan, R.Y.A., Mulchandani, A.: Electrochemical Impedance Spectroscopy (EIS): Principles, Construction, and Biosensing Applications. Sensors. 21, 6578 (2021). https://doi.org/10.3390/s21196578

89. Lumetzberger, J., Buchner, M., Pile, S., Ney, V., Gaderbauer, W., Daffé, N., Moro, M.V., Primetzhofer, D., Lenz, K., Ney, A.: Influence of structure and cation distribution on magnetic anisotropy and damping in Zn/Al doped nickel ferrites. Phys. Rev. B. 102, (2020). https://doi.org/10.1103/physrevb.102.054402

90. Prithivirajan, P., Lavanya, N., Ravindran, B., Jasmine, S., Thirupathy, J., Dhas, S., Chithambaram, V.: Silver-substituted cobalt ferrite nanoparticles' characteristics for energy storage and magnetic devices applications. J Mater Sci: Mater Electron. 37, (2026). https://doi.org/10.1007/s10854-026-16635-z

91. Ragheb, R., Nobbmann, U.: Multiple scattering effects on intercept, size, polydispersity index, and intensity for parallel (VV) and perpendicular (VH) polarization detection in photon correlation spectroscopy. Sci Rep. 10, 21768 (2020). https://doi.org/10.1038/s41598-020-78872-4

92. Farkas, N., Kramar, J.A.: Dynamic light scattering distributions by any means. J Nanopart Res. 23, (2021). https://doi.org/10.1007/s11051-021-05220-6

93. Austin, J., Minelli, C., Hamilton, D., Wywijas, M., Jones, H.J.: Nanoparticle number concentration measurements by multi-angle dynamic light scattering. J Nanopart Res. 22, (2020). https://doi.org/10.1007/s11051-020-04840-8

94. Zhdanov, V.P.: Diffusion-limited association of nanoparticles in fluid: Beyond the no-slip boundary conditions. Colloid and Interface Science Communications. 46, 100538 (2021). https://doi.org/10.1016/j.colcom.2021.100538

95. Meulendijks, N., Van Ee, R., Stevens, R., Mourad, M., Verheijen, M., Kambly, N., Armenta, R., Buskens, P.: Flow Cell Coupled Dynamic Light Scattering for Real-Time Monitoring of Nanoparticle Size during Liquid Phase Bottom-Up Synthesis. Applied Sciences. 8, 108 (2018). https://doi.org/10.3390/app8010108

96. Levin, A.D., Sadagov, A.Y., Shchelkonogov, V.A., Sinebryukhova, A.M.: Estimation of the Dimensions of Nanoparticles in Multicomponent Colloidal Sysems by Dynamic Light Scattering. Meas Tech. 60, 1091–1096 (2018). https://doi.org/10.1007/s11018-018-1323-7

97. Wang, Y., Li, G., Zhang, Y., Li, L.: Zinc Ferrite Nanoparticles: Unusual Growth Mechanism for Size-Dependent Properties. ChemistrySelect. 6, 1862–1869 (2021). https://doi.org/10.1002/slct.202004562

98. Georgieva, M., Tzankov, D., Kovacheva, D., Tumbalev, V., Karadimov, T., Setzer, A., Esquinazi, P., Georgiev, P.A.: Magnetism vs microstructure in Zn-substituted Ni-ferrite nanocrystalline materials with potential for biomedical applications. J. Phys. D: Appl. Phys. 59, 025006 (2026). https://doi.org/10.1088/1361-6463/ae3090

99. Desai, Y.P., Jamwal, S., Modiyil, S., Chodankar, S., Sathe, R., Kothawale, M.M.: Structural and magnetic studies of nanocrystalline Ni-Zn ferrites synthesized by sol-gel method. In: AIP conference proceedings. p. 030511. Cornell University (2020)

100. Bobade, D.H., Mane, A.T., Mane, A.T., Shinde, D.P., Bagwan, S.: Effect of Annealing Temperature on the Structural, Magnetic, and Morphological Properties of Mg-Ni-Zn Ferrite Nanoparticles. IJRIAS. 10, 389–398 (2025). https://doi.org/10.51584/ijrias.2025.10060025

101. Yu, Q., Su, Y., Tursun, R., Zhang, J.: Synthesis and characterization of low density porous nickel zinc ferrites. RSC Adv. 9, 13173–13181 (2019). https://doi.org/10.1039/c9ra01076a

102. Sutka, A., Gross, K.A., Mezinskis, G., Bebris, G., Knite, M.: The effect of heating conditions on the properties of nano- and microstructured Ni–Zn ferrite. Phys. Scr. 83, 025601 (2011). https://doi.org/10.1088/0031-8949/83/02/025601

103. Rayar, A., Prasanna, G.D.: Synthesis and characterization of zinc doped nickel nanoferrites via sol-gel auto-combustion technique. IOP Conf. Ser.: Mater. Sci. Eng. 1300, 012046 (2024). https://doi.org/10.1088/1757-899x/1300/1/012046

104. Khangembam, S., Victory, M., Surchandra, W., Phanjoubam, S.: Electrical and structural properties of zinc substituted nickel ferrites synthesized by sol-gel technique. Advanced Materials Proceedings. 2, 162–166 (2021). https://doi.org/10.5185/amp.2017/306

105. Abdullah Dar, M., Shah, J., Siddiqui, W.A., Kotnala, R.K.: Study of structure and magnetic properties of Ni–Zn ferrite nano-particles synthesized via co-precipitation and reverse micro-emulsion technique. Appl Nanosci. 4, 675–682 (2013). https://doi.org/10.1007/s13204-013-0241-x

106. Vinnik, D.A., Zhivulin, V.E., Sherstyuk, D.P., Starikov, A.Y., Zezyulina, P.A., Gudkova, S.A., Zherebtsov, D.A., Rozanov, K.N., Trukhanov, S.V., Astapovich, K.A., Sombra, A.S.B., Zhou, D., Jotania, R.B., Singh, C., Trukhanov, A.V.: Ni substitution effect on the structure, magnetization, resistivity and permeability of zinc ferrites. J. Mater. Chem. C. 9, 5425–5436 (2021). https://doi.org/10.1039/d0tc05692h

107. Jovanović, S., Yaacoub, N., Slimani, S., Kržmanc, M.M., Vukomanović, M., Spreitzer, M., Peddis, D., Omelyanchik, A.: Effect of Zn-substitution on magnetic structure of cobalt ferrite nanoparticles. The Journal of chemical physics. 161, (2024). https://doi.org/10.1063/5.0226884

108. Gomes, R.C., Pilati, V., Martins, F.H., Silva, F.G.D., Gomide, G., Pereira, B.C.C., Coppola, P., Oliveira Paula, F.L., Campos, A.F.C., Kern Barreto, C., Goya, G.F., Porcher, F., Aquino, R., Dubois, E., Perzynski, R., Depeyrot, J.: Decoding magnetization and magnetic anisotropy in core@shell ferrite nanoparticles: interplay between cation distribution and spin disorder. Nanoscale. (2026). https://doi.org/10.1039/d6nr00200e

109. Babu, Y.R.: Effect of Mg substitution on the magnetic properties of Ni–Zn ferrites. Pramana - J Phys. 88, (2017). https://doi.org/10.1007/s12043-017-1393-0

;

Figure

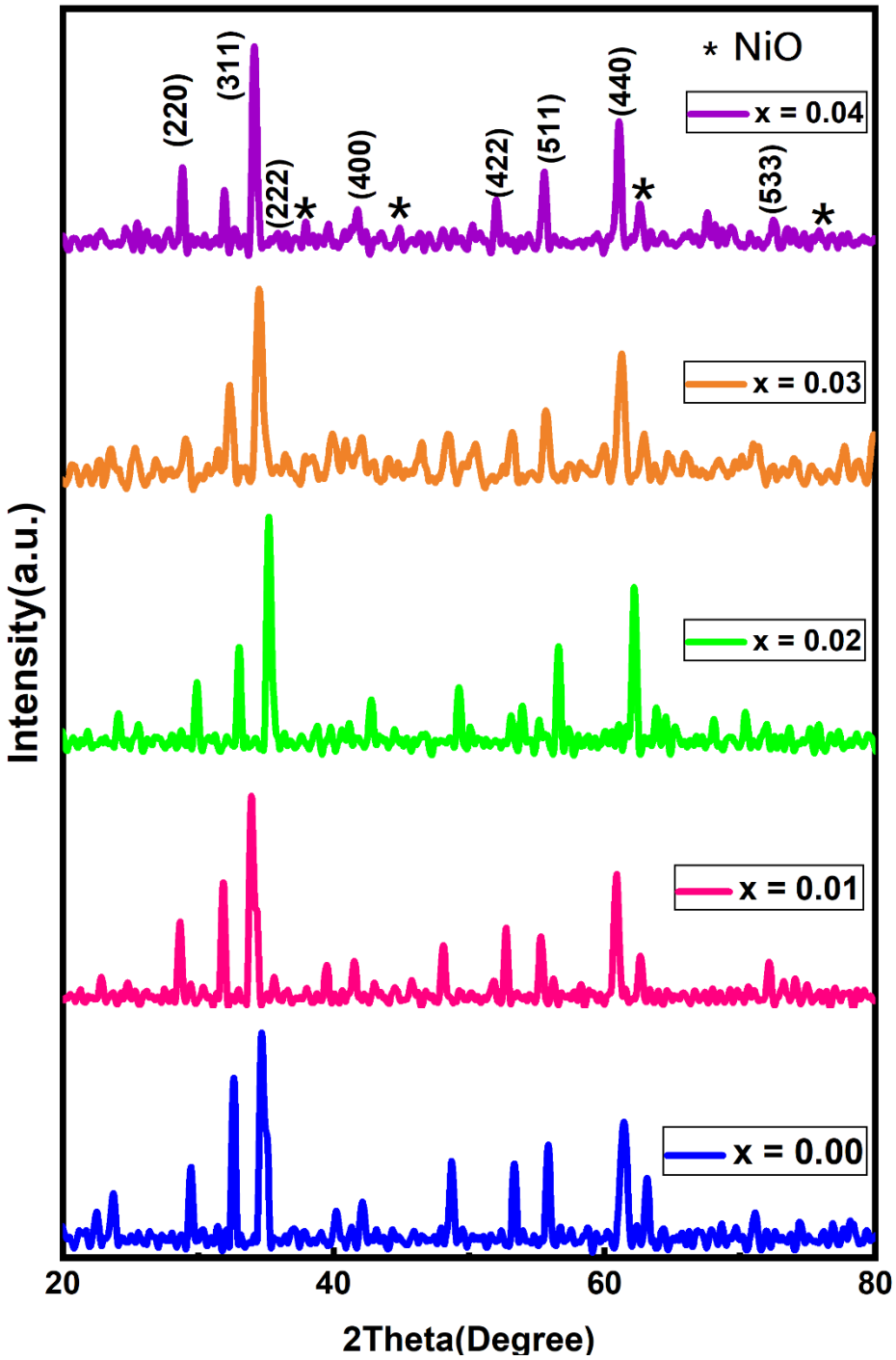


Figure 1. X-ray diffraction (XRD) patterns of the synthesized $Zn_{1-x}Ni_xFe_2O_4$ ($0.0 < x < 0.04$) nanoparticles, illustrating the formation of the single-phase face-centered cubic spinel structure

and the evolution of the prominent (311) crystallographic reflection with varying nickel concentrations.

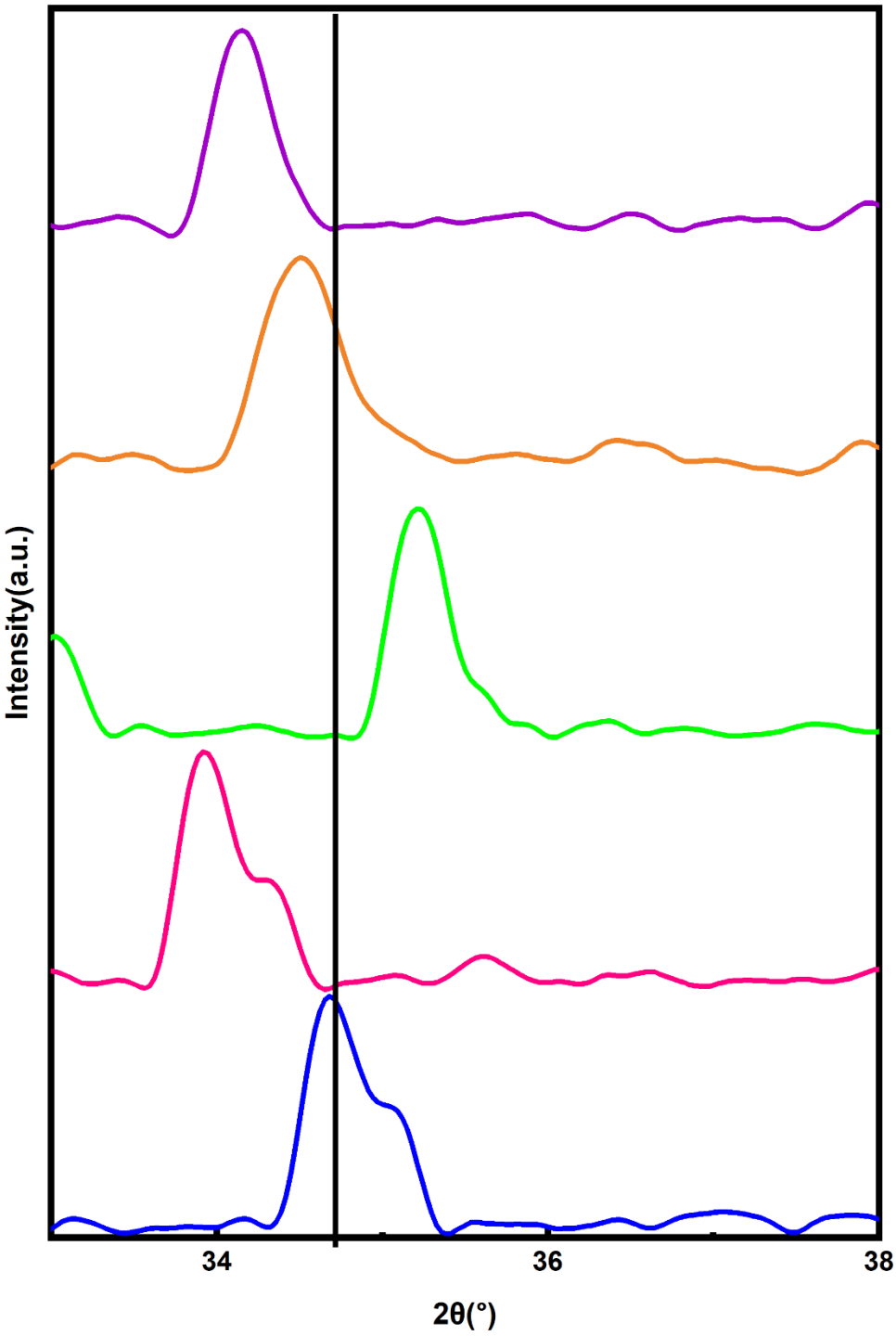


Figure 2. elucidated enlarge view the evolution of the prominent (311) crystallographic reflection with varying nickel concentrations.

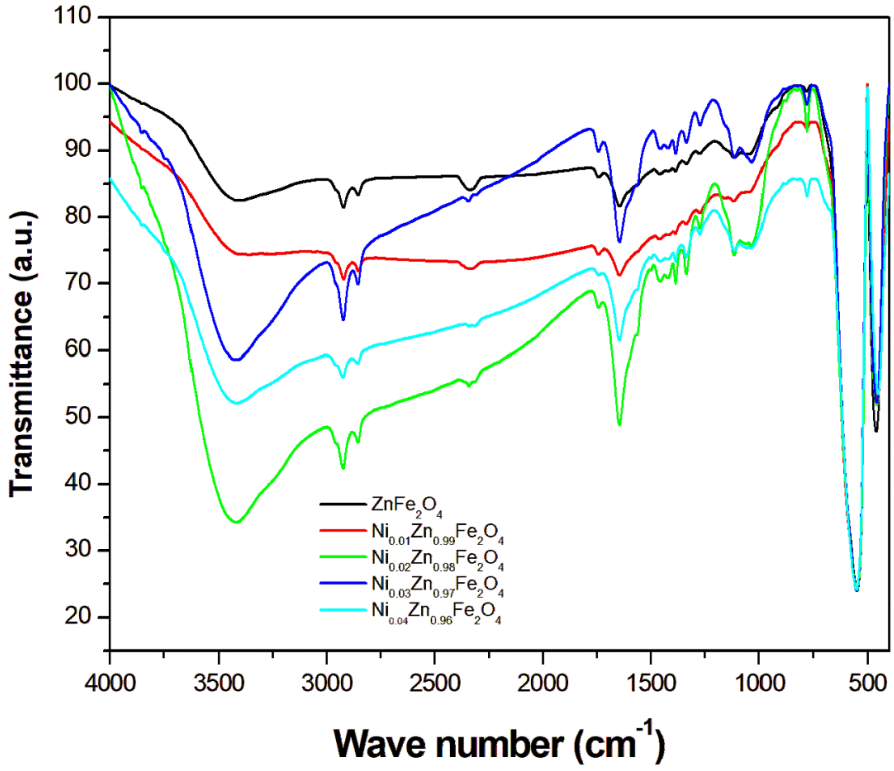


Figure 3. Fourier transform infrared (FTIR) spectra of the $Zn_{1-x}Ni_xFe_2O_4$ (x = 0.00 to 0.04) nanoparticles recorded in the wavenumber range of 4000–400 cm-1, highlighting the characteristic tetrahedral (ν1) and octahedral (ν2) metal-oxygen stretching vibrations alongside the surface-adsorbed functional groups.

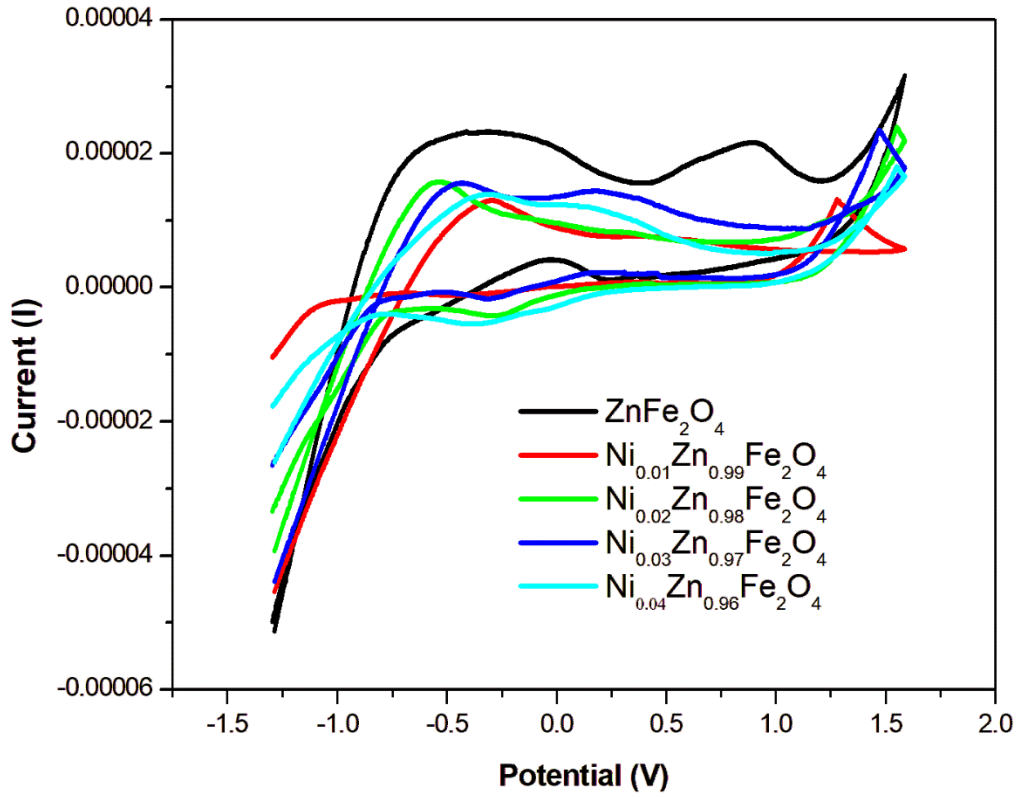


Figure 4. Cyclic voltammograms (CV) of the $Zn_{1-x}Ni_xFe_2O_4$ ($0.0 < x < 0.04$) nanoparticle electrodes measured at a constant scan rate of 10 mV/s, demonstrating the distinct faradaic redox peaks and the significantly enhanced specific capacitance achieved at optimal Ni2+ substitution levels.

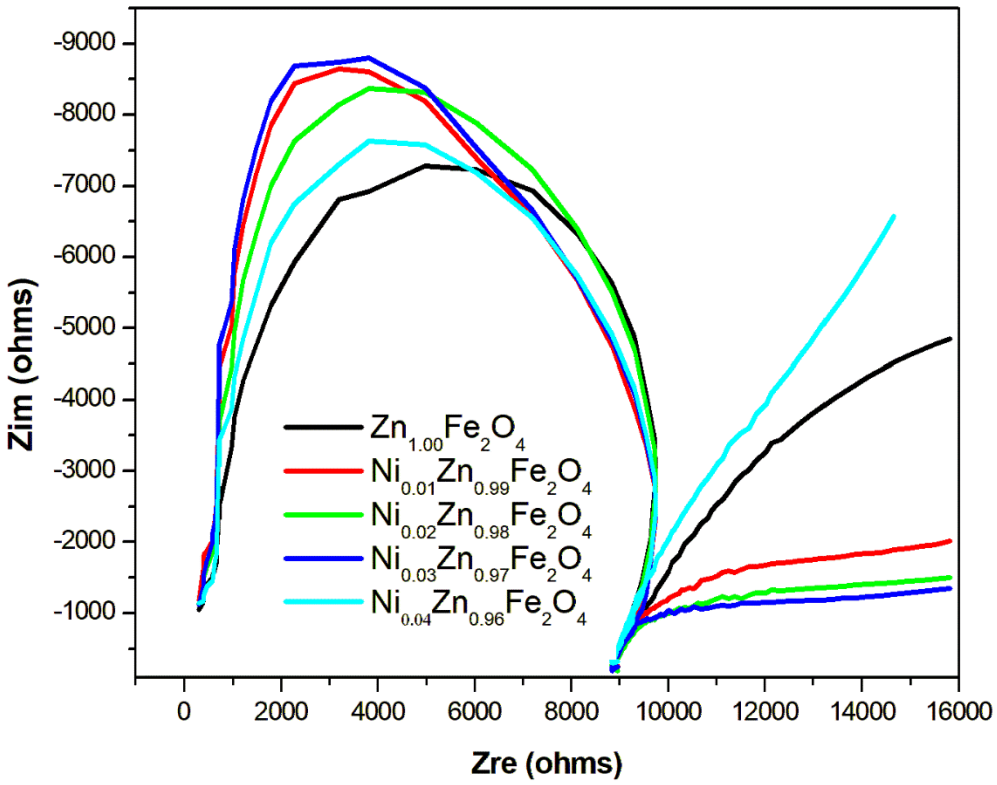


Figure 5. Nyquist plots (Zim vs. Zre) derived from the electrochemical impedance spectroscopy (EIS) of the annealed $Zn_{1-x}Ni_xFe_2O_4$ (x = 0.00 to 0.04) nanoparticles, displaying the fitted depressed semicircles that confirm grain boundary-dominated charge transport mechanisms and non-ideal relaxation behavior.

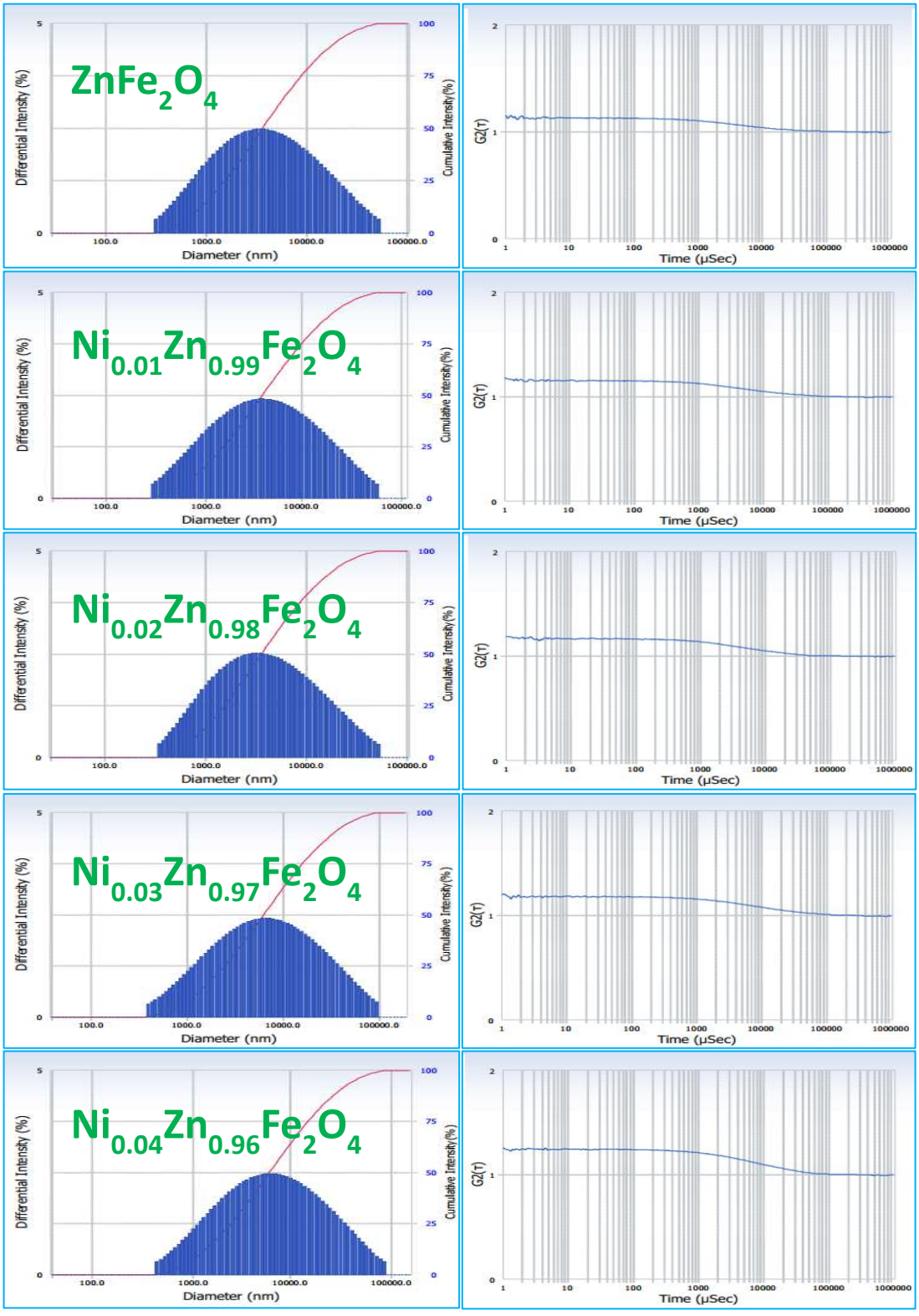

ZnFe2O4
Ni0.01Zn0.99Fe2O4
Ni0.02Zn0.98Fe2O4
Ni0.03Zn0.97Fe2O4
Ni0.04Zn0.96Fe2O4
Differential Intensity (%)
Cumulative Intensity (%)
Diameter (nm)
G2(τ)
Time (µSec)

Figure 6. Dynamic light scattering (DLS) hydrodynamic size distribution profiles (Differential Intensity vs. Cumulative Intensity) for the aqueous dispersions of $Zn_{1-x}Ni_xFe_2O_4$ ($0.0 < x < 0.04$) nanoparticles, providing quantitative evidence of the macroscopic secondary agglomeration driven by high surface-to-volume ratios.

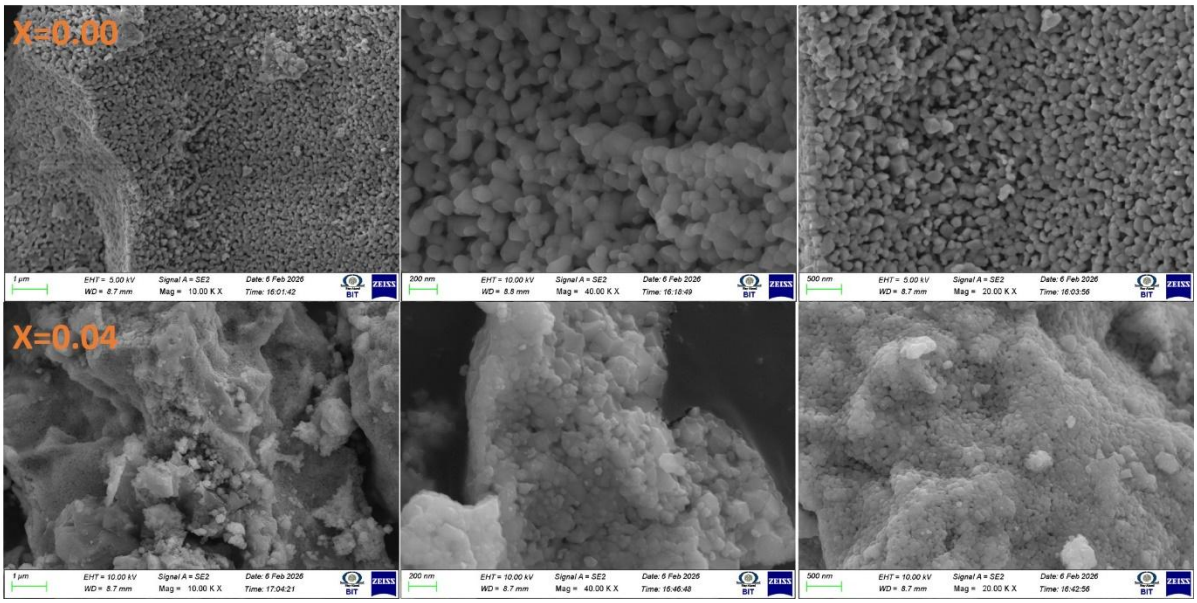


Figure 6. Field emission scanning electron microscopy (FE-SEM) micrographs of the pristine ($x = 0.00$) and highly doped ($x = 0.04$) zinc ferrite nanoparticles captured across multiple magnifications (1 μm, 500 nm and 200 nm), revealing the highly porous, spherical structural morphology and the extensive interconnected agglomeration network.

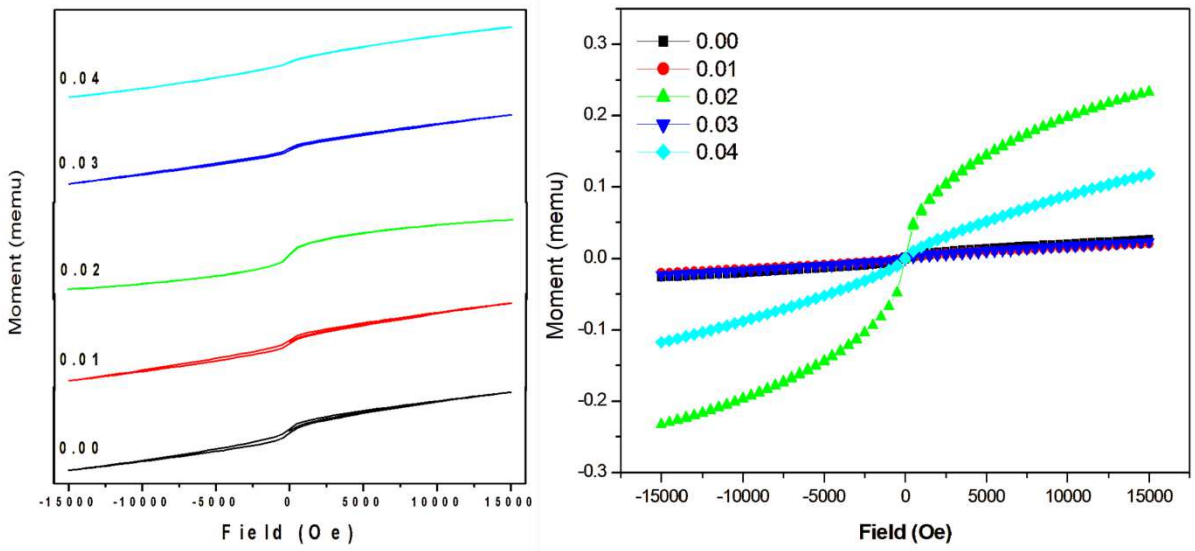


Figure 7. Room-temperature magnetic hysteresis (M-H) loops of the synthesized $Zn_{1-x}Ni_xFe_2O_4$ nanoparticles, demonstrating the concentration-dependent variations in saturation magnetization and magnetic coercivity driven by Ni^{2+} substitution and nanoscale microstructural confinement.

Supplementary Files

This is a list of supplementary files associated with this preprint. Click to download.

- Tabledocx.docx